JGR Oceans

RESEARCH ARTICLE
10.1029/2025JC023751

Key Points:

- Biphase and nonlinear energy transfer are studied across a wide range of offshore wave conditions and foreshore slopes
- In shallow water, energy at the peak frequency (50%) and higher harmonics (50%) contribute to energy transfer to lower harmonics
- Non-hydrostatic models accurately and efficiently capture wave statistics, including higher order statistics

Supporting Information:

Supporting Information may be found in the online version of this article.

Correspondence to:

M. P. de Ridder,
menno.deridder@deltares.nl

Citation:

de Ridder, M. P., Mares-Nasarre, P., & van Gent, M. R. A. (2026). Wave energy transfer in shallow water: Numerical investigation of slope and offshore wave condition effects. *Journal of Geophysical Research: Oceans*, *131*, e2025JC023751. https://doi.org/10.1029/2025JC023751

Received 17 NOV 2025
Accepted 4 AUG 2026

Author Contributions:

Conceptualization: M. P. de Ridder
Data curation: M. P. de Ridder
Formal analysis: M. P. de Ridder
Funding acquisition: M. R. A. van Gent
Investigation: M. P. de Ridder
Methodology: M. P. de Ridder
Project administration: M. R. A. van Gent
Software: M. P. de Ridder
Supervision: P. Mares-Nasarre, M. R. A. van Gent
Validation: M. P. de Ridder
Visualization: M. P. de Ridder
Writing – original draft: M. P. de Ridder

Wave Energy Transfer in Shallow Water: Numerical Investigation of Slope and Offshore Wave Condition Effects

M. P. de Ridder[1,2], P. Mares-Nasarre[1], and M. R. A. van Gent[1,2]

[1]Department of Hydraulic Engineering, Delft University of Technology, Delft, The Netherlands, [2]Department of Coastal Structures and Waves, Deltares, Delft, The Netherlands

Abstract This study advances the understanding of nonlinear wave interactions in shallow water by numerically quantifying how foreshore slope and offshore conditions influence energy transfer and wave evolution over a broad range of conditions. Two non-hydrostatic models, SWASH and XBeach, are validated against physical experiments and applied across a wide range of conditions. The two-layer SWASH model accurately reproduces wave parameters, third-order statistics, and nonlinear energy transfer. Results show that the relative water depth (kh), the offshore wave steepness ($s_{m-1,0,\mathrm{deep}}$) and the Iribarren number (ξ) are key parameters for describing the interaction strength and biphase behavior. The slope mainly affects high-frequency biphase behavior, whereas for the other nonlinear interactions it primarily alters the magnitude of the energy transfer. For ξ smaller than 0.2, low-frequency energy is redistributed toward higher frequencies within the surf zone, while low-frequencies at steeper slopes only receive energy. In shallow water ($kh < 0.5$), energy transfer to higher and lower frequencies is not dominated solely by primary wave interactions. Triads involving two high-frequency components $\left(f > 1.5 f_p\right)$ and one low-frequency component play a major role, alongside interactions of one low-frequency component with two primary components. Consequently, milder slopes increase low-frequency wave height contributions up to 60%, whereas steeper slopes result in 20%–40% for the studied conditions. High-frequency contributions remain relatively stable across profiles and offshore conditions, accounting for approximately 60%–70% of total wave height in shallow water.

Plain Language Summary The characteristics of a wave field change significantly when waves propagate from deeper water to shallow water. Numerical models can be used to obtain accurate nearshore wave conditions. In this study, two so-called non-hydrostatic wave models are validated based on physical flume experiments. Both the transformation of the wave parameters and the wave properties that describe the wave shape are accurately reproduced by the numerical models. The best performing model is then applied to study how the wave energy is redistributed or dissipated for a large set of wave conditions and foreshore slopes. Based on these numerical simulations, it is observed that energy from frequencies around the peak frequency is transferred to lower and higher frequencies, as found by previous studies. However, in shallow water, energy from frequencies higher than the peak frequencies also contributes to the energy increase at lower frequencies. Considering the foreshore slope, different results are found for mild and steep sloping profiles. These changes in energy redistribution also affect the wave parameters. For mild foreshore slopes, the wave height of the low-frequency components can become significant, whereas this is less remarkable for the higher frequencies.

1. Introduction

Wave hydrodynamics undergoes significant changes when waves propagate from deep water to shallow water. Due to changes in the water depth, waves start shoaling and refract toward the shoreline (as first described by Lamb, 1932). Next to shoaling and refraction, the wave shape becomes nonlinear as the water depth decreases due to nonlinear processes (e.g., Stoker, 1992). When the wave shape becomes too nonlinear, waves become unstable and begin to break, causing their energy to dissipate (e.g., Peregrine, 1983). The nonlinear wave shape observed in the nearshore zone is a result of energy transfer between different frequency components, leading to the generation of bound waves at both higher and lower frequencies relative to the primary wave (e.g., Freilich & Guza, 1984; Longuet-Higgins & Stewart, 1962). In the surf zone, this behavior can be physically interpreted by the fact that the wave crest propagates faster than the trough, causing an asymmetrical wave profile and contributing to frequency redistribution. Energy is transferred within the wave spectrum mainly by triad interactions in shallow water, as these triad interactions are only significant in shallow water depth (e.g., Hasselmann, 1962). The energy redistribution to lower frequencies results in low-frequency waves (LF

Writing – review & editing: P. Mares-Nasarre, M. R. A. van Gent

waves, e.g., Battjes et al., 2004; Janssen et al., 2003; Longuet-Higgins & Stewart, 1962), and the energy redistribution to higher frequencies results in higher harmonics (HH waves), causing the nonlinear wave shape (e.g., De Wit et al., 2020; Elgar & Guza, 1985a, 1985b; Freilich & Guza, 1984). Several studies suggest that most energy is dissipated in the higher frequency tail and that energy transfers to higher frequencies are the dominant sink of wave energy at lower frequencies (De Bakker et al., 2015; Hasselmann, 1962; Rijnsdorp et al., 2022). For mild foreshore slopes, it is observed that low-frequency components can become nonlinear and thereby dissipate energy (e.g., De Bakker et al., 2014; S. M. Henderson et al., 2006; Van Dongeren et al., 2007), but it is also shown that energy at low frequencies can transfer back to the higher frequencies deep in the surf zone (De Bakker et al., 2016; Rijnsdorp et al., 2014). Norheim et al. (1998) showed that on gentle foreshore slopes, both higher and lower frequencies, gain more energy than at steeper foreshore slopes. It has also been shown that energetic conditions result in relatively more energy transfer than milder conditions (De Bakker et al., 2015; Herbers & Guza, 1994; Norheim et al., 1998). Next to the bound wave generation mechanism (e.g., Longuet-Higgins & Stewart, 1962; Padilla & Alsina, 2017) for lower frequencies, the varying breakpoint is the dominant mechanism for steeper slopes (Baldock & Huntley, 2002; Symonds et al., 1982).

After waves are broken due to a shallow water depth, the wave shape changes significantly over a short distance, classified as the inner surf zone by Svendsen et al. (1978). These breaking waves become non-dispersive (Martins et al., 2021; Thornton & Guza, 1982) and transform into a sawtooth-shaped signal as a result of a balance between dissipation and nonlinearity (Bonneton, 2023). In addition, within the surf zone, the bound LF waves are released and become free propagating low-frequency waves with a phase lag which deviates from the deep water (where it is 180°) as the largest short waves only exist on top of a low-frequency wave (e.g., Janssen et al., 2003).

Thus, several processes affect the hydrodynamics in shallow water. As the wave height reduces due to wave breaking, an (artificial) shallow foreshore in front of a coastal sea defense can be applied to enhance the coastal safety against flooding (e.g., Van den Hoven et al., 2023; Van Gent & Teng, 2023; Vuik et al., 2016). However, it is important to understand how a foreshore affects the nearshore hydrodynamics, especially as the nonlinear transfer of energy could potentially result in unwanted effects (e.g., higher LF waves). Moreover, it is also important to accurately model these phenomena to design, for example, a sandy foreshore efficiently.

Non-hydrostatic wave models have been shown to model nearshore wave hydrodynamics efficiently (i.e., Al Khalili et al., 2025; De Ridder et al., 2021; Smit et al., 2014; Zijlema et al., 2011) with validation studies using, among others, physical model experiments (i.e., Al Khalili et al., 2025; De Bakker et al., 2016; Rijnsdorp et al., 2014) and field measurements (e.g., C. S. Henderson et al., 2022). These models incorporate nonlinear processes, unlike spectral wave models, yet remain computationally efficient for simulating larger domains compared to detailed CFD models. Thus, these models are suitable to characterize the hydrodynamics at a foreshore, as also demonstrated by Lashley et al. (2020). In addition to bulk parameters, an increasing number of studies focus on nonlinear energy transfer and third-order statistics to better understand the underlying processes (e.g., De Bakker et al., 2016; Fiedler et al., 2019; Rijnsdorp et al., 2014; Ruju et al., 2019; Smit et al., 2014; Torres-Freyermuth et al., 2010). Both Smit et al. (2014) and De Bakker et al. (2016) validated the nonlinear energy transfer term itself, showing the potential of applying these models to obtain a better understanding of nearshore wave conditions. Fiedler et al. (2019) explored various methods to force a numerical model based on measurements including validation of higher-order statistics of low-frequencies and several studies have explored the low-frequency transformation (e.g., De Bakker et al., 2016; Mendes et al., 2018; Ruju et al., 2019). The first objective of this paper is to broaden the validation to a wider range of conditions through physical model experiments. By using physical model experiments, two commonly applied non-hydrostatic wave models, SWASH and XBeach-nh, are validated for extreme shallow water dynamics.

The second objective is to explore the hydrodynamics for a large set of conditions using the preferred numerical model. Previous studies have investigated hydrodynamics and energy transfers between frequencies at the foreshore using numerical models (e.g., Rijnsdorp et al., 2022, for LF waves), physical experiments (e.g., De Bakker et al., 2015; Martins et al., 2021), and field measurements (e.g., Herbers et al., 2000). However, these studies typically focus on one or a few wave conditions and profile shapes, either numerically or experimentally. Field studies often cover a broader range of wave conditions, but are generally less systematic. This study focuses on numerically modeled hydrodynamics, third-order statistics, and energy transfers for a large range of wave conditions and profile shapes, extending the work of, for example, Fiedler et al. (2019) and Rijnsdorp et al. (2022). By defining frequency-integrated bulk energy transfers for low frequencies $\left(f < f_p/2\right)$, high frequencies $\left(f > 1.5f_p\right)$, and primary frequencies $\left(1.5f_p > f > f_p/2\right)$, the energy transfer for higher harmonics and low-frequency components is analyzed for a large set of conditions. These simulations are used to examine how offshore wave conditions and profile slope influence the characteristics of low- and high-frequency components, leading to a classification relevant for engineering purposes.

The paper is structured as follows. In Section 2, the parameters and applied theories are defined. In Section 3 the validation of the numerical models, including the third-order statistics and the nonlinear energy transfers is described. In Section 4, the preferred settings and numerical model are applied to a large set of wave conditions to show how the third-order statistics and nonlinear energy transfer vary. Section 5 contains a discussion of the results, and the conclusions are given in Section 6.

2. Hydrodynamics

2.1. Wave Parameters

The bulk wave parameters are computed based on the spectral wave moments defined as,

$$m_n = \int_{f_{\min}}^{f_{\max}} f^n E(f) df \tag{1}$$

where f is the frequency, $f_{\min}$ the minimum frequency, $f_{\max}$ the maximum frequency, n the power and $E(f)$ the energy density. Based on the spectral moments, the wave height $\left(H_{m0} = \sqrt{4m_0}\right)$ and the spectral period $\left(T_{m-1,0} = \frac{m_{-1}}{m_0}\right)$ are computed. To distinguish between various regions in the wave spectrum, the frequency range bounded by $f_{\min}$ and $f_{\max}$ is set to $0 - f_p/2$ (LF components), $f_p/2 - 1.5f_p$ (Primary components) and $1.5f_p - f_{\text{nyq}}$ (HH components) with f_p the peak frequency at deep water and f_{nyq} the Nyquist frequency. The combined frequency range of the primary waves and higher harmonics $\left(f > f_p/2\right)$ is defined as HF components. Third order statistics are quantified with the wave asymmetry (A_s) and skewness (S_k) defined as,

$$A_s = \frac{\langle \mathcal{H}(\eta^3) \rangle}{\langle \eta^2 \rangle^{3/2}} \tag{2}$$

$$S_k = \frac{\langle \eta^3 \rangle}{\langle \eta^2 \rangle^{3/2}} \tag{3}$$

where $\mathcal{H}(\cdot)$ is the Hilbert transform and η is the free surface elevation time series. To quantify the correlation between various frequency bands in the wave spectra, the approach suggested by Fiedler et al. (2019) is applied and extended with a higher harmonics frequency band, resulting in the following band-filtered time series,

$$\eta = \eta_{LF} + \eta_p + \eta_{HH} \tag{4}$$

Based on this definition, the non-normalized skewness is given by,

$$\begin{aligned}\langle \eta^3 \rangle = \langle \eta_{LF}^3 \rangle + 3\langle \eta_{LF}\eta_p^2 \rangle + 3\langle \eta_{LF}^2\eta_p \rangle + 6\langle \eta_{LF}\eta_p\eta_{HH} \rangle + 3\langle \eta_{LF}^2\eta_{HH} \rangle +\\ 3\langle \eta_{LF}\eta_{HH}^2 \rangle + \langle \eta_p^3 \rangle + 3\langle \eta_p^2\eta_{HH} \rangle + 3\langle \eta_p\eta_{HH}^2 \rangle + \langle \eta_{HH}^3 \rangle\end{aligned} \tag{5}$$

where each term represents a contribution to the total non-normalized skewness. In a similar way the asymmetry for each term is computed. Each term represents a potential interaction between the signals, as these terms are only nonzero for signals with phase correlations and zero for a signal with random phases. A nonzero value does not necessarily imply an interaction between the wave components. For example, the correlation between short waves and LF waves in the surf zone could be the result of more wave breaking of short waves in the trough of the LF wave compared to the crest. Based on these definitions, the biphase $\left(\phi_{*,*,*}\right)$ and bicoherence $\left(B_{*,*,*}\right)$ are computed with,

$$\phi_{*,*,*} = \arctan\left(\frac{As_{*,*,*}}{Sk_{*,*,*}}\right) \tag{6}$$

$$B_{*,*,*} = \sqrt{As^2_{*,*,*} + Sk^2_{*,*,*}} \tag{7}$$

where $*,*,*$ indicates which signals are used (e.g., LF,p,p represents $\eta_p^2\eta_{LF}$). For correlations within a single frequency band (e.g., $\eta_{p,p,p}$), the biphase characterizes the wave shape: a value of 90° corresponds to pitch-forward, sawtooth-like waves, while 0° indicates peaky waves (see Appendix A). In contrast, the biphase of cross-frequency correlations between two signals (e.g., $\phi_{p,p,LF}$) reflects the time lag between them. The bicoherences represent the strength of the correlation. To compare various wave conditions, the bicoherence is normalized with the approach described in Fiedler et al. (2019) with values between 0 and 1 with larger values representing stronger correlation. For a low bicoherence, the biphase tends to be randomly distributed. Therefore, biphase values are not computed for bicoherence levels below 0.02. In Appendix A, the transformation in $\phi_{*,*,*}$ and $B_{*,*,*}$ over a sloping foreshore are illustrated for a bichromatic wave group.

All the third-order statistics are computed in the time domain, but to show the distribution of the third-order statistics, the bispectrum is computed, defined as (Hasselmann et al., 1963),

$$B(f_1, f_2) = \langle A_{f_1} A_{f_2} A^*_{f_1+f_2} \rangle \tag{8}$$

where A_{f_1} is the complex Fourier component at frequency f, $\langle\cdot\rangle$ the mean operator and * represents the complex conjugate. Using 46 Hann-windowed blocks with 50% overlap and averaging over 2×2 squares, we obtain a degrees of freedom of 184 (with $\Delta f = 0.02Hz$), which is consistent with values reported in previous studies (e.g., Elgar & Guza, 1985a; Martins et al., 2021).

Spectral properties, both co-spectrum and energy density, are computed using Welch's method (Welch, 1967) using a segment of 4,000 points for the validation and with 50% overlap ($\Delta f = 0.025Hz$, degrees of freedom of approximately 270). Also, the mean water level ($\langle\eta\rangle$), computed as the mean value over the last 60 s and the 2% exceedance value of the wave height ($H_{2\%}$) are computed.

2.1.1. Wave Energy Balance

To understand the energy redistribution within a spectrum, a frequency-resolved energy balance is used, given by,

$$\frac{\partial E_f}{\partial t} + \frac{\partial F_f}{\partial x} = S_{nl,f} + S_{\mathrm{fric},f} + S_{\mathrm{diss},f} \tag{9}$$

where E_f is the energy, F_f is the energy flux, $S_{nl,f}$, the nonlinear energy transfer, $S_{\mathrm{fric},f}$ dissipation by bottom friction and $S_{\mathrm{diss},f}$ represents all other dissipation (e.g., turbulence) given at frequency f. In a stationary sea state, the first term is zero, and the energy flux is balanced by the dissipative terms and the nonlinear energy transfer term. Two energy balances are applied. An energy balance based on the Boussinesq scaling (a/h small and same order as kh with a the amplitude, h the water depth and k the wave number), and a fully nonlinear energy balance based on the nonlinear shallow water equations is applied in the surf zone (a/h small and dispersive effects are neglected, $kh \ll 1$) are applied. Bed shear stress is neglected in this balance and may contribute to a non-closing residual. However it is expected to be relevant only in very small water depths, such as wave runup, which is not modeled in this study.

For weakly nonlinear waves, the energy balance based on the Boussinesq scaling can be applied (e.g., De Bakker et al., 2015; Herbers & Burton, 1997; Herbers et al., 2000), with the energy flux defined as,

$$F_{x,f} = \frac{\partial F_f}{\partial x} = \frac{\partial c_g E_{in,f}}{\partial x} \tag{10}$$

and the $S_{nl,f}$ is computed in the time domain as (Equation C2 in S. M. Henderson et al., 2006),

$$S_{nl,f} = \frac{-3\pi f}{h} I\big(\mathrm{C}(\eta^2;\eta)\big) \tag{11}$$

where c_g is the group velocity ($\sqrt{gh}$ for Boussinesq assumption), $E_{in,f}$ the incident energy (Computed using Sheremet et al., 2002), f the frequency, h the water depth, $I(\cdot)$ the imaginary part and $\mathrm{C}(\cdot)$ the cospectrum. For nonlinear waves in shallow water, the non-dispersive balance based on the nonlinear shallow water equations given by Rijnsdorp et al. (2022) can be applied, where the energy flux is given by,

$$F_{x,f} = \frac{\partial F_f}{\partial x} = g\mathrm{C}(hu;\eta) + g\mathrm{C}(\eta u;\eta) + 0.5\mathrm{C}(huu;u) \tag{12}$$

and the nonlinear energy transfer is given by,

$$S_{nl,f} = 0.5\left(\mathrm{C}\left(Duu;\frac{du}{dx}\right) - \left(\mathrm{C}\left(Du;u\frac{du}{dx}\right) + 0.5g\left(\mathrm{C}\left(\eta u;\frac{d\eta}{dx}\right) - \left(\mathrm{C}\left(u;\eta\frac{d\eta}{dx}\right)\right.\right.\right.\right. \tag{13}$$

where h is the water depth, u the depth averaged velocity and D instantaneous water depth $(h + \eta)$. Note that in Rijnsdorp et al. (2022), the velocity is defined both at the cell center and cell face, whereas here the velocity is always defined at the cell center.

Boussinesq scaling is only valid for weakly nonlinear waves with the Ursel number $\left(a/h/(kd)^2\right)$ of order $O(1)$ and fairly long waves ($kh < 1$). The non-dispersive balance is valid for highly nonlinear waves in shallow water with Ursel number larger than 1 and $kh < 1$. Moreover, the frequency resolving balance is only valid for slowly varying wave amplitudes (so called WKB assumption) and the energy flux term should include the incident wave energy.

To distinguish between different triads, $S_{nl,f}$ is computed for various combinations of band-filtered signals (LF, p, and HH), similar to the approach used for bicoherence and biphase. Rather than integrating specific regions of the bispectrum (e.g., De Bakker et al., 2015), a time-domain analysis is applied, following Rijnsdorp et al. (2022) (Consistency between both method is discussed in Appendix B). All combinations with the same triad are combined into the $S_{nl,f,*,*,*}$. For example, $S_{nl,f,p,p,LF}$ contains all the possible combinations of the three band filtered signals (u_*, u_* and $\frac{du_*}{du_*}$ with $*$ represents LF, p or HH) in the cospectrum in Equation 13, and represents the nonlinear energy transfer of a triad between two primary waves and one LF wave. These results are summed over the three frequency bands to obtain the bulk nonlinear source terms,

$$S_{nl,LF|*,*,*} = \sum_{f=0}^{f<f_p/2} S_{nl,f,*,*,*} \tag{14}$$

$$S_{nl,p|*,*,*} = \sum_{f>f_p/2}^{f<1.5f_p} S_{nl,f,*,*,*} \tag{15}$$

$$S_{nl,HH|*,*,*} = \sum_{f>1.5f_p}^{f<f_{nyq}} S_{nl,f,*,*,*} \tag{16}$$

where $*,*,*$ represents the three frequency bands. These terms represent the total energy transfer from or toward a frequency band (e.g., LF) for a specific triad of wave components (e.g., LF, p, p).

3. Validation

3.1. Model Setup

The commonly applied non-hydrostatic models XBeach-nh (De Ridder et al., 2021) and SWASH (Zijlema et al., 2011) are compared with results from physical model experiments described in De Ridder et al. (2024). In

Table 1
Overview of Variations in Numerical Simulations

Model	Vertical discretization	Breaker parameter	Other
SWASH	2-layers	0.6	–
SWASH	2-layers	0.6	First order steering
SWASH	10-layers	–	–
xb-nh	Reduced 2-layers	0.4	–

these experiments, approximately 1,000 irregular waves propagate over a sloping foreshore (slopes 1/100, 1/50, and 1/20) with a horizontal part after the slope ending with a wave absorber at the end of the flume. In SWASH a vertical discretization needs to be specified, whereas XBeach has a reduced 2-layer model as vertical discretization (or one layer). While the reduced two-layer model in XBeach offers improved representation of dispersive wave behavior compared to a single-layer model, it remains less accurate than a fully two layer model. The domains are discretized with a horizontal resolution of 60 points per offshore peak period wavelength, and output is requested at 75 equidistant points with a time step of 0.01 s. The default breaker parameters are applied, 0.4 for XBeach and 0.6 in SWASH (i.e., Den Bieman et al., 2024; Roelvink et al., 2018; Smit et al., 2013). The model boundary is positioned at the first wave gauge, where the incident signal from this wave gauge is forced. This incident signal is defined as a high-pass filtered measured signal combined with a decomposed low-frequency measured signal. This is necessary because offshore reflection coefficients range between 10% and 30%, with the highest reflections occurring during conditions with significant low-frequency energy generation, which is not perfectly absorbed at the end of the flume. The second-order boundary condition, as proposed and implemented by Vasarmidis et al. (2024), is applied in SWASH to transform the free surface elevation to the layer-averaged velocity using the model dispersion relation. A similar approach is applied for XBeach, but without the correction for the numerical dispersion relation for second-order waves. A sponge layer with a length of 7 m is applied at the back boundary to mimic the wave absorber as applied in the experiments.

Next to the 2-layer SWASH model, a 10-layers SWASH model and a 2-layer SWASH model without the LF waves at the boundary (*ADDBoundwave* removed from input file) are applied (see Table 1). Variations in the vertical discretization will show the effects of dispersive behavior, and the simulations without LF waves will indicate how important it is to include these waves in the boundary signal. The 10-layer simulation is applied without breaker formulation, as a multi-layer model should capture the correct wave shape (Smit et al., 2013).

Fourteen tests are used as validation with variations in offshore wave height ($H_{m0,\text{target}}$), offshore wave steepness ($s_{m-1,0,\text{deep}}$), water depth (h_{deep}) and foreshore slope (m, see Table 2). At five locations in the flume, wave measurements are available where at two of the five locations a set of multiple wave gauges is placed to decompose the signals (see Figure 1). See De Ridder et al. (2024) for a complete description of the model campaign.

3.2. Results

3.2.1. Validation Results

To illustrate the wave propagation over a relatively gentle foreshore slope ($m = 1:100$), the results for Test CA711 are shown in Figure 2. For this particular test, the offshore wave height reduces by approximately 30% over the foreshore slope and the low-frequency wave height increases from 0.01 to 0.03 m. Results for simulations with the two different slopes and two different offshore steepness are shown Appendix C.

Figure 2 shows the short-wave height ($H_{m0,HF}$), low-frequency wave height ($H_{m0,LF}$), wave setup ($\langle\eta\rangle$), short-wave spectral period ($T_{m-1,0,HF}$), asymmetry (A_s), skewness (S_k), 2% exceedance wave height ($H_{2\%}$), bicoherence of two primary components and one LF or HH component ($B_{p,p,LF}$ and $B_{p,p,HH}$) and the biphase of a triad with two primary components and one LF component ($\phi_{p,p,pLF}$). Overall, the models accurately capture the wave parameters, consistent with findings from previous studies (e.g., Rijnsdorp et al., 2014; Smit et al., 2014). Both shoaling and the breaking point are accurately captured. The low-frequency growth (Panel b), and the wave shape transformation (Panel e) matches the experiments, showing that the nonlinear processes are also reproduced. The

Table 2

Tests Conditions From De Ridder et al. (2024) Applied to Validate the Numerical Models Where m Represents the Foreshore Slope, $H_{m0,\text{target}}$ the Target Wave Height, T_p the Target Peak Period, $s_{m-1,0}$ the Wave Steepness $(2\pi H_{m0}/(gT^2_{m-1,0}))$ and h_{deep} the Offshore Water Depth

TestID	m [−]	$H_{m0,\text{target}}$ $[m]$	T_p $[s]$	h_{deep} $[m]$	$s_{m-1,0}$ [−]
CA411	1:100	0.10	1.88	0.90	0.015
CA413	1:100	0.10	1.15	0.90	0.025
CA911	1:100	0.10	1.88	0.55	0.04
CA921	1:100	0.15	2.30	0.55	0.015
CA913	1:100	0.10	1.15	0.55	0.04
CA923	1:100	0.15	2.30	0.55	0.04
CC911	1:20	0.10	1.88	0.55	0.015
CC913	1:20	0.10	1.15	0.55	0.04
CC711	1:20	0.10	1.88	0.63	0.015
CC713	1:20	0.10	1.15	0.63	0.04
CA711	1:100	0.10	1.88	0.63	0.015
CA713	1:100	0.10	1.15	0.63	0.04
CB911	1:50	0.10	1.88	0.55	0.015
CB913	1:50	0.10	1.15	0.55	0.04

correct wave shape is reflected in a good match for $B_{p,p,LF}$ and $B_{p,p,HH}$ (Panel g). In the surf zone, the wave height reduction also matches the observations both for the 2% exceedance wave height, low-frequency wave height and short wave height. The biphase of the low-frequencies changes in the surf zone from 180° to approximately −50° both numerically as in the observations. The strength of the correlation between two primary waves and one low-frequency (LF) or one higher harmonic (HH) decreases in the surf zone, which is also observed in physical experiments. The largest differences arise in the surf zone ($x > 30$ m) mainly for the $H_{m0,LF}$, S_k and A_s. Note that the transformation from $x = 45$ m is caused by the sponge layer.

The 10-layer model shows a larger reduction of $H_{m0,HF}$ in the surf zone, resulting in a different wave shape (Panel e) and spectral period (Panel d). The simulation without the LF energy at the offshore boundary shows similar results for most of the variables, except for the $H_{m0,LF}$ and $B_{p,p,LF}$. The $H_{m0,LF}$ is underestimated offshore and overestimated nearshore, as a result of a free spurious free wave. At the boundary this spurious wave is out of phase with the bound wave canceling the bound wave at the boundary. As both waves travel with a different speed, both components appear in the domain increasing the total LF energy nearshore for the simulation with both the spurious free and bound wave. This free spurious wave also affects the $B_{p,p,LF}$ with an overestimation offshore. Also, $\phi_{p,p,LF}$ is slightly different at the wave boundary for the simulations without LF waves at the boundary. The results between XBeach and SWASH are very similar. Similar results were found for the other simulations, see also Appendix C.

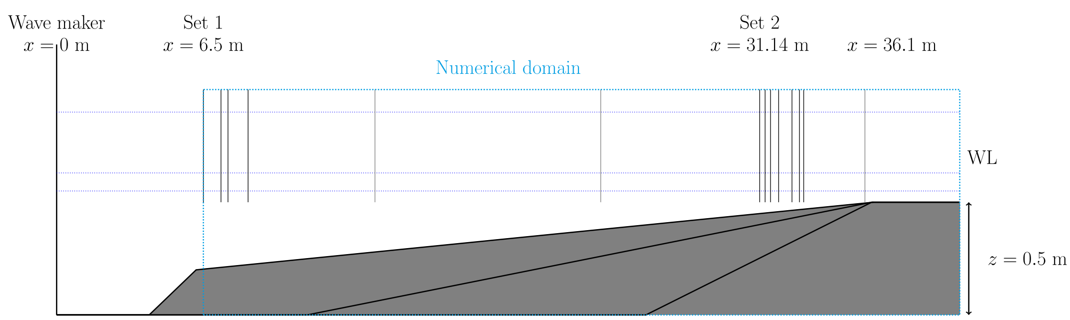

Figure 1. Schematic overview of the physical model experiments as described in De Ridder et al. (2024). Wave gauges as part of a set are shown in black. The gray instruments represent wave gauges that are not part of a set.

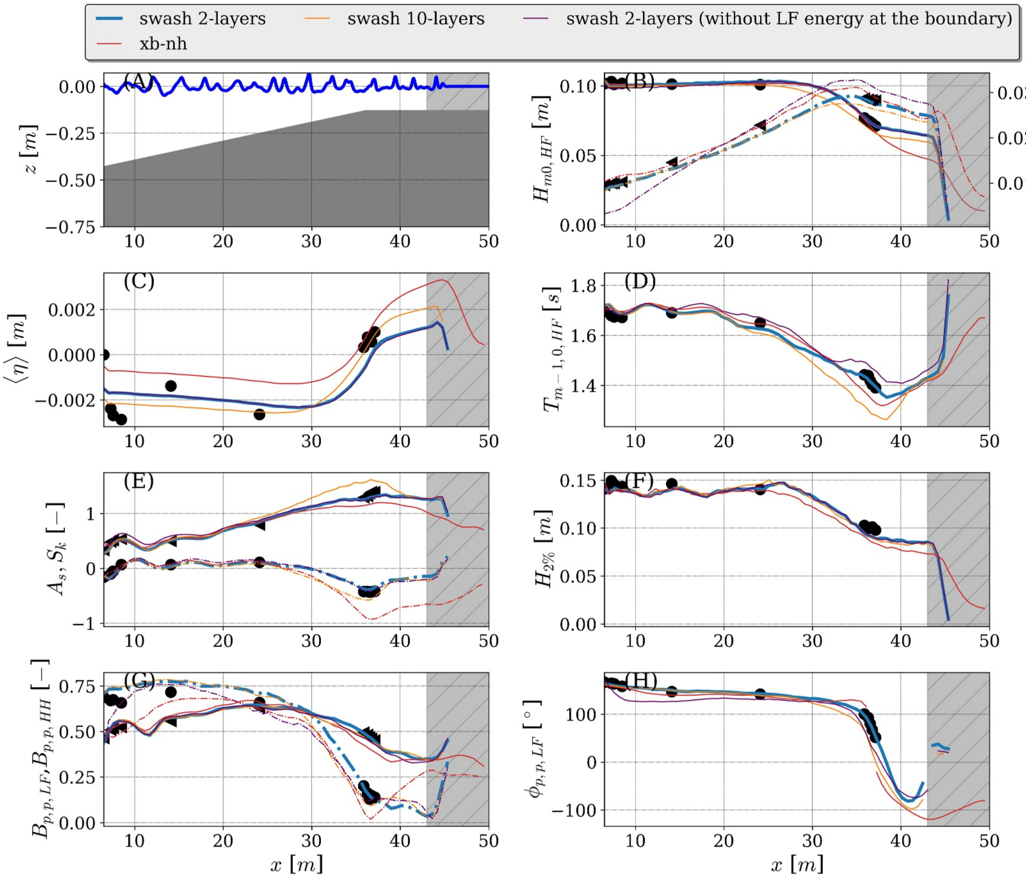

Figure 2. Comparison of short wave height ($H_{m0,HF}$, Panel b), low-frequency wave height ($H_{m0,LF}$, Panel b, dashed lines), wave setup ($\langle\eta\rangle$, Panel c), short wave spectral period ($T_{m-1,0,HF}$, Panel d), wave asymmetry (A_s, Panel e), wave skewness (S_k, Panel e, dashes lines), 2% exceedance wave height ($H_{2\%}$, Panel (f), bicoherence of signal involving two primary waves and one low-frequency wave ($B_{p,p,LF}$, Panel g), bicoherence of signal involving two primary waves and one higher harmonic ($B_{p,p,HH}$, Panel g, dashed lines) and biphase of signal involving two primary waves and one low-frequency wave ($\phi_{p,p,LF}$, Panel h) for various models for Test CA711. The black dots show the observations from the wave flume experiments. The low-frequency height, skewness and $B_{p,p,HH}$ are shown with a dashed line and triangles for the observations. The sponge layer is indicated with gray shaded area.

To demonstrate the accuracy of the spectral shape, the wave spectra are compared for several locations in the wave flume in Figure 3. A different test (Test CC711 with a steep 1 : 20 foreshore slope) than that shown in Figure 2 is chosen as the changes in the spectral shape are more pronounced for this test. Both the dissipation of wave energy at the peak and the nonlinear energy transfer to higher and lower harmonics are accurately captured by the different models. The SWASH-10 layer model shows slightly better results for the high-frequency tail in deep water due to the better dispersive behavior (Panels d and e), especially for deep water conditions. The simulations without low-frequencies at the boundary show a large deviation at the offshore boundary for the lower frequencies, but the error decreases for shallower locations in the domain. Thus, all the considered models are able to simulate the spectral shape accurately for the tested conditions.

This test clearly demonstrates the nonlinear energy transfer within the spectrum with an increased energy at the lower frequencies and the higher frequencies (Panel f). The correlation between components and the nonlinear energy transfer is visible in the bispectrum (Panels a–c). At lower frequencies, red regions in the imaginary part of the bispectrum (lower triangle) indicate energy gain at these frequencies. As a result, the bicoherence, $B_{p,p,LF}$, between two primary waves and one low-frequency (LF) wave increases, with the strongest bicoherence (0.61) observed in Panel B for this simulation. Regarding nonlinear energy transfer to higher frequencies, the highest bicoherence ($B_{p,p,HH}$) is found in Panel c. In the bispectrum, this is visible as a blue patch near the peak frequency, indicating that energy is transferred from this frequency to higher frequencies. Also at two times the peak

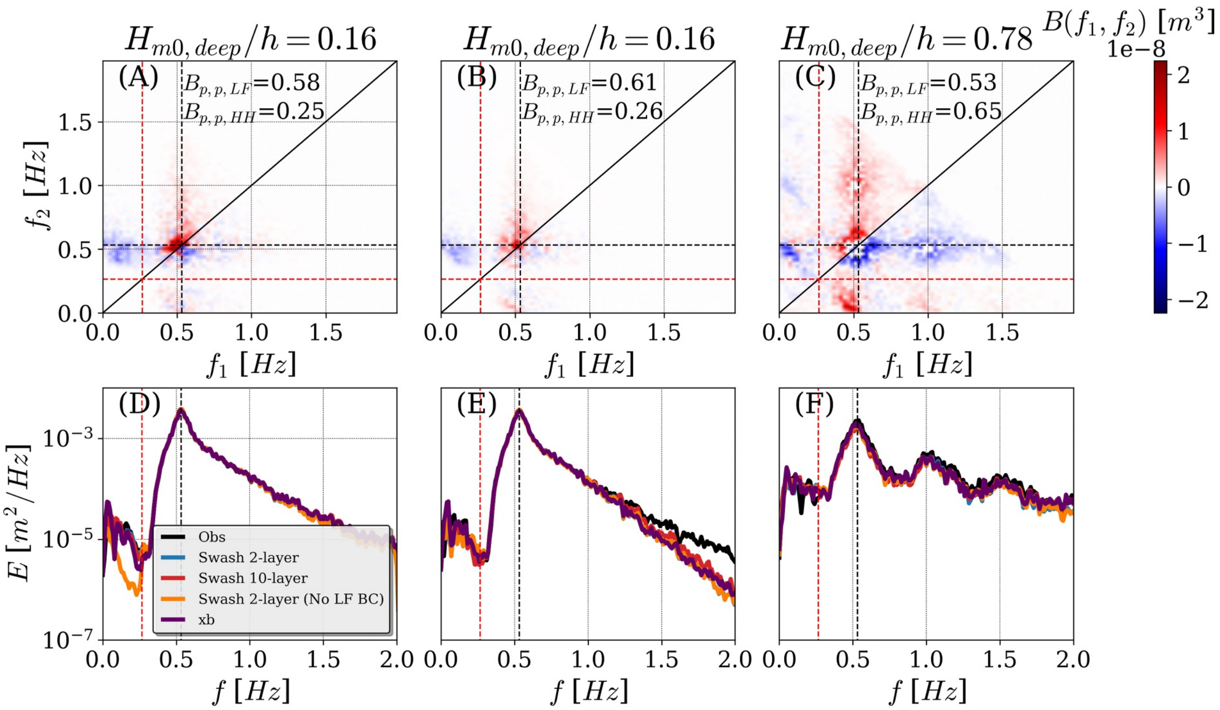

Figure 3. The upper panels (Panels a–c) show the bispectrum for various locations, where the upper triangle represents the real part and the lower triangle the imaginary part. The lower panels (d–f) show the energy density spectra for various simulations at three different locations. The peak of the spectrum is indicated with a dashed black line and the dashed red line represents the $f_p/2$. Results are obtained from test CC711.

frequency, a blue patch is present showing that also energy at $2f_p$ is transferred to higher harmonics $(3f_p)$. In the spectrum, this is visible as second and third-order peaks.

3.2.2. Overview Validation

The statistical measures of all the simulations are presented in Figure 4 for different wave parameters. The left axis displays the Scatter Index (SCI) and the Relative bias (Rel. bias) (blue and red bars), while the right axis shows the coefficient of determination R^2 (cyan bar). Here, R^2 serves as a normalized error metric whereas, the SCI and rel. bias quantify the relative measure for the scatter. These measures are defined as follows:

$$\text{SCI} = \sqrt{\frac{\langle x - \langle x \rangle \rangle - \langle y - \langle y \rangle \rangle}{\langle y \rangle}} \tag{17}$$

$$\text{Rel. Bias} = \frac{\sum (x - y)}{\sum y} \tag{18}$$

$$R^2 = 1 - \frac{\sum (y - x)^2}{\sum (y - \langle y \rangle)^2} \tag{19}$$

where x is the modeled value and y the observed value. A higher SCI indicates greater scatter, while a higher Rel. Bias reflects a larger deviation. The R^2 ranges from ∞ to 1, with 1 indicating a perfect match between model and observations.

The first panel shows the incident wave height at the first set of wave gauges, calculated using the decomposition method from De Ridder et al. (2023). This confirms that the correct wave energy is forced at the model boundary with a R^2 larger than 0.95 for the four models. Visual inspection of the offshore time series also validates the match between the time series (see Appendix D).

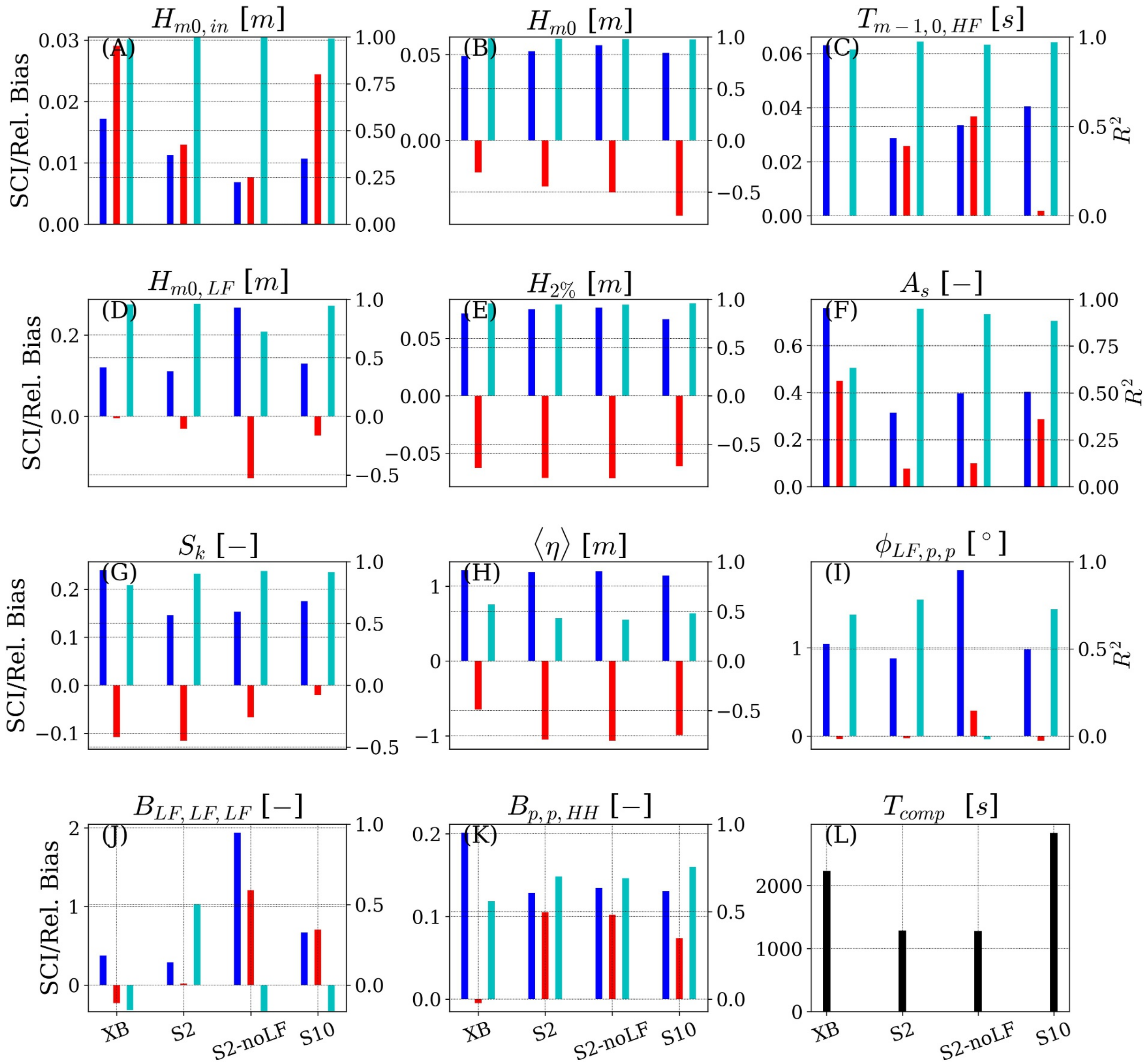

Figure 4. Bar plots with the scatter index (blue bar, left axis), relative bias (red bar, left axis) and r-squared (cyan bar, right axis) for various wave parameters in each subplot for several simulations (x-axis). T_{comp} represents the mean computational time. Panel (a) shows the incident wave height, Panel (b) shows the wave height, Panel (c) the short wave spectral period, Panel (d) the low-frequency wave height, Panel (e) the 2% exceedance wave height, Panel (f) the asymmetry, Panel (g) the skewness, Panel (h) the wave setup, Panel (i) the biphase of the low-frequency wave and two primary waves, Panel (j) the bicoherence of low-frequency components, Panel (k) the bicoherence of two primary components and a high-frequency component and Panel (l) the mean computation time.

XBeach and SWASH (2-layers) show comparable performance for the wave parameters (H_{m0}, $T_{m-1,0,HF}$, $H_{m0,LF}$ and $H_{2\%}$) with R^2 larger than 0.95. However, differences become more apparent in third-order statistics, where SWASH 2-layer performs better, particularly for the A_s, S_k, $B_{p,p,LF}$ $B_{p,p,HH}$, and $B_{LF,LF,LF}$. The slightly better dispersive behavior with the 2-layer SWASH model results in a better representation of the nonlinear wave properties compared to the reduced two-layer approach in XBeach. Although the offshore boundary in this test set is not located in very deep water (large kh), limiting the impact of dispersion, simulations with higher kh values show that the 10-layer SWASH model better resolves the high-frequency tail, but the effect on wave parameters is limited.

The inclusion of the low-frequency (LF) waves at the boundary significantly affects the $H_{m0,LF}$, $\phi_{LF,p,p}$ and $B_{LF,LF,LF}$. Due to the mismatch at the boundary, spurious free waves, out of phase with the bound waves, are generated, affecting mainly the total magnitude of the LF waves ($H_{m0,LF}$) with an underestimation offshore and

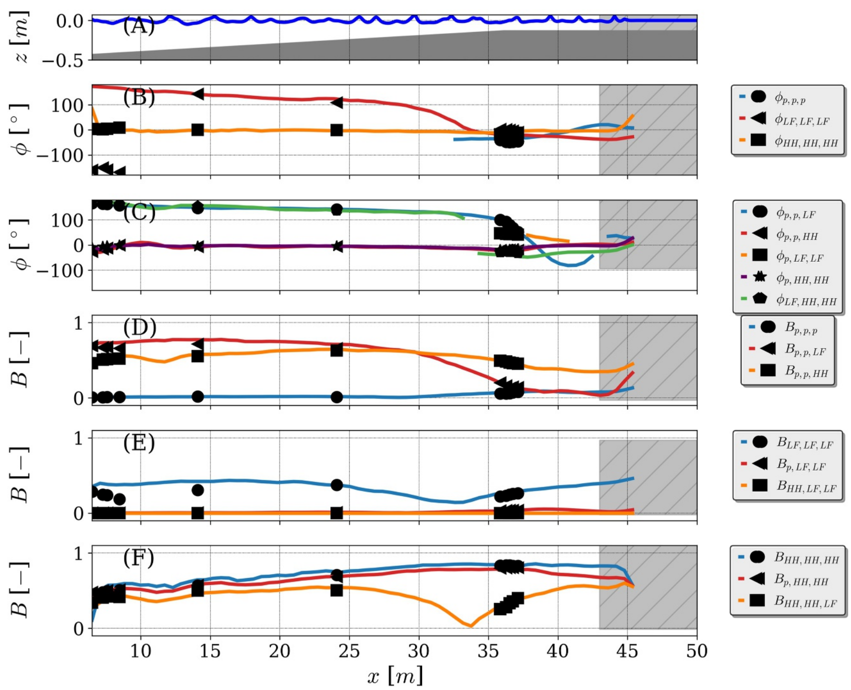

Figure 5. Biphase $(\phi_{*,*,*})$ and bicoherence $(B_{*,*,*})$ for Test CA711 computed over several correlations between low-frequency components (LF), primary components (p), and higher harmonics (HH). The bathymetry and instantaneous free surface elevation is shown in Panel (a). Panel (b) shows the biphase over different frequency ranges and Panel (c) shows the biphase over cross-frequency correlations. Panels (d–f), show the bicoherence of the various correlations. The black symbols represent the results from the wave gauges in the physical model experiments. The results are only shown for a bicoherence larger than 0.02. The sponge layer is indicated with a gray shaded area.

overestimation nearshore. Next to the $H_{m0,LF}$, also the bichoherence is less accurate as the free spurious waves reduce the correlation.

Not only is the accuracy important, but also the computational time is considered. The computation time, including writing of output and post-processing, is verified. All simulations are performed serial with Intel Xeon Gold machines with 2.80 GHz. The 10-layer SWASH model requires most of the computational time, with a mean computational time of 2,800 s. The two SWASH 2-layer simulations has a mean computation time of 1,250 s. Remarkably, the XBeach model also requires a significant computational time (mean of 2,200 s), although it was expected to be faster than SWASH 2-layer. A reason for this deviation could be the reading/writing of data of the model. It must also be noted, that the added value of the reduced 2-layers in XBeach on the computational time is mainly significant for 2D simulations, where solving for the non-hydrostatic pressure is very time consuming.

Given its accuracy and lower computational cost, including for third-order statistics, the 2-layer SWASH model is selected for further use in this study.

3.2.3. Third-Order Statistics and Nonlinear Energy Transfer

In addition to the validation presented in the previous section, the various possible bicoherences and biphases are assessed using physical model experiments. Also, the total amount of energy transfer, based on the Boussinesq formulation, is verified. Results from the SWASH 2-layer model and a single test case are presented in Figures 5 and 6 to illustrate the model's accuracy in capturing both third-order statistics and nonlinear energy transfer between various triads, based on the Boussinesq formulation. Statistical scores of three important parameters are included in Figure 4.

As the summation of the nonlinear energy transfer over the frequencies of a triad integrates to zero (indicating redistribution rather than gain or loss), the summation over the absolute values is shown, which represents the

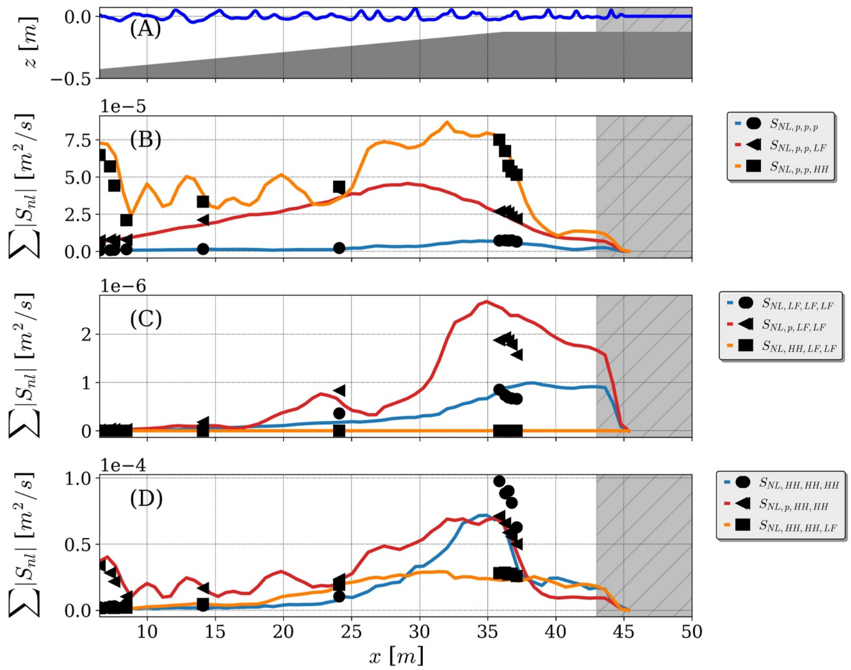

Figure 6. The absolute value of the nonlinear energy transfer ($S_{nl,f}$) summed over all the frequencies for various triads as a function of the location in the flume. Results are shown for Test CA711. The bathymetry and instantaneous free surface elevation is shown in Panel (a). Panel (b) shows the interactions involving two or three primary components ($p, p, *$), Panel (c) shows the interactions involving two or three low-frequency components ($LF, LF, *$) and Panel (d) shows the interactions involving two or three higher harmonics ($HH, HH, *$). The sponge layer is indicated with a gray shaded area.

magnitude of the nonlinear energy transfer. It should be noted that the experiment duration is relatively short (approximately 1,000 waves), limiting the reliability of the nonlinear energy transfer estimates, both numerically and in the experiments. Furthermore, only the Boussinesq formulation is considered, as it does not depend on the depth-averaged velocity, which is not measured at multiple locations in the flume. This validation is performed to demonstrate the accuracy of the nonlinear energy transfer obtained with the numerical model, but does not show the accuracy of the Boussinesq formulation itself.

These results show how the energy is transferred in the spectrum and how this affects the wave shape. In the shoaling zone ($x \approx 30$ m), the LF components are out of phase with the primary wave group $\left(\phi_{p,p,LF} = 180°\right)$ with a strong correlation ($B_{p,p,LF} > 0.75$). Up until the breakpoint, the energy transfer between two primary components and one LF component, increases (Panel b of Figure 6). Around $x \approx 25$m, not only the primary components transfer energy to the LF component, but also the triad involving two HH components and one LF component becomes important (Panel d in Figure 6) with also a biphase of 180°. In contrast to $B_{p,p,LF}$, the bicoherence of this triad ($B_{HH,HH,LF}$) increases from the boundary toward the break point (Panel f in Figure 5). When the primary waves start breaking ($x \approx 34$m), the energy transfer reduces, for both $S_{nl,p,p,LF}$ and $S_{nl,HH,HH,LF}$ (Panel b and d in Figure 6). The biphase turns from 180° toward −90° as in shallow water, only primary component can exist on top of the crest of a LF components. Due to this correlation in shallow water, the bicoherence of the triad increases again, but not the energy transfer.

Within the LF frequency region, energy is transferred, but this is only significant in the surf zone where $S_{LF,LF,LF}$ increases (Panel c of Figure 6). In the shoaling zone, the $B_{LF,LF,LF}$ is fairly constant and drops at the break point after which it increases again in the surf zone. Similarly to $\phi_{p,p,LF}$, $\phi_{LF,LF,LF}$ is 180° in the shoaling zone and becomes −10° in the surf zone, showing that the shape of the LF signal changes as the water depth decreases.

The forcing of higher order harmonics indicated by $B_{p,p,HH}$ increases in the shoaling zone, which is mainly caused by the energy transfer between two primary components and one HH component (Panel b in Figure 6). Compared to the energy transfer to lower frequencies, the energy transfer toward higher frequencies is significantly larger and does not decrease in the surf zone. Moreover, these HH components do not have a phase-lag with the

Table 3
Overview of the Variations Applied in the Simulations Where m Represents the Foreshore Slope, H_{m0} the Wave Height, s_0 the Steepness Based on the Peak Period $\left(2\pi H_{m0}/\left(gT_p^2\right)\right)$

H_{m0} $[m]$	0.1, 0.15 and 0.2
s_0 $[-]$	0.01, 0.025 and 0.04
h $[m]$	1.1
profiles:	
A	$m = 0.005$
B	$m = 0.01$
C	$m = 0.02$
D	$m = 0.05$
E	$m = 0.07$
F	$m = 0.1$
G	tanh shape ($m \approx 0.02$)
H	tanh shape ($m \approx 0.05$)

corresponding primary components, indicated by a $\phi_{p,p,HH}$ of approximately zero. The $B_{HH,HH,HH}$ also shows that there is energy transfer within the HH region with an increasing $B_{HH,HH,HH}$ and $S_{nl,HH,HH,HH}$ in the surf zone (Panel f of Figure 5 and Panel d of Figure 6). Close to the boundary, oscillations in the $S_{nl,p,p,HH}$ and $B_{p,p,HH}$ are observed. These may result from mismatches between the boundary signal and the numerical solution. The use of two vertical layers assumes a depth-averaged velocity, which could generate spurious high-frequency waves and standing wave patterns close to the boundary. These spurious waves have wavelengths different to the bound waves, causing a spatially standing wave pattern which is reflected in the bicoherence and nonlinear energy transfer.

Overall, the numerical simulations match well with the observations of the third-order statistics both, in the shoaling zone and in the surf zone. Both the biphase $\left(\phi_{*,*,*}\right)$ and the bicoherence $(B_{*,*,*})$ of the various frequency bands are very similar to the observed values. Only the LF signal $(B_{LF,LF,LF})$ shows a small deviation close to the boundary $(x = 0$ m) with a larger bicoherence $(B_{LF,LF,LF})$ and a biphase $\left(\phi_{LF,LF,LF}\right)$ with the opposite sign (Panels b and e). It is not known what causes this difference, but it is observed for several simulations. The absolute amount of energy transfer in the spectrum is also relatively well captured with the model (see Figure 6), as also previously demonstrated in for example, Smit et al. (2014). Here only the total amount of energy transfer in the triad with two LF signals and one primary signal $(S_{nl,p,LF,LF})$ shows an overestimation (Panel c in Figure 6) and $S_{nl,HH,HH,HH}$ is slightly overestimated. These findings show that various nonlinear energy transfers are important in shallow water, affecting the wave shape, and that the numerical model SWASH is able to capture these processes.

4. Hydrodynamics at Foreshore

The SWASH-2 layer model is applied to analyse hydrodynamics under varying wave conditions and profile geometries (see Table 3), including six linear slopes and two hyperbolic tangent-shaped profiles. Two hyperbolic-shaped profiles were included to show how the profile shape affects the hydrodynamics. The horizontal distance of the hyperbolic-shaped profiles are based on the slope $(z(x) = \tanh(x/(0.2L_x))$ with $L_x = 1/\mathrm{m}\Delta z$ and $\Delta z = 1$ m). All profiles start at 1 m depth and end with a 10 m horizontal part with a water depth of 0.1 m to allow wave energy absorption at the back boundary. The grid resolution is given by a uniform grid with a resolution of 60 points per wavelength based on the peak wavelength.

Compared to the physical model experiments described in De Ridder et al. (2024), the number of profiles is extended and the numerical model makes it possible to obtain output for a larger set of wave gauges to obtain insights into the physics. Moreover, the duration of these simulations is longer than in the physical model experiments to obtain a more reliable estimate for the spectral properties.

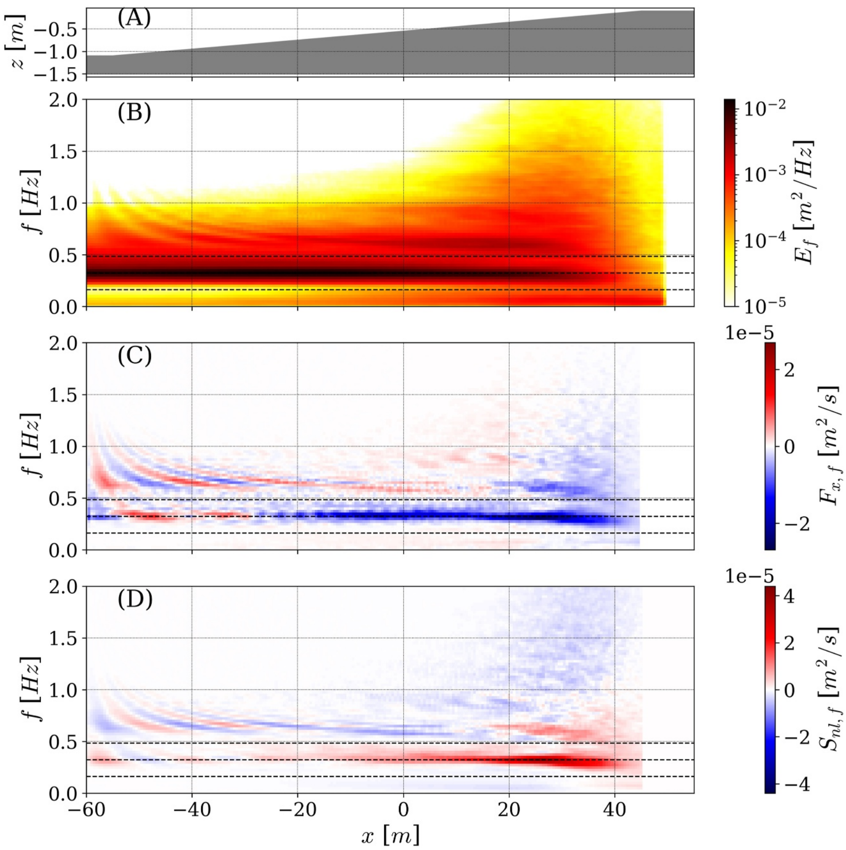

Figure 7. Domain of simulation (Panel a), energy density (E_f, Panel b), gradient in energy flux (F_x,f, Panel c) and nonlinear energy transfer ($S_{nl,f}$, Panel d) for Test B121 ($H_{m0} = 0.15m$, $s_0 = 0.01$ and $m = 0.01$) computed with the Boussinesq theory (Equations 10 and 11) as function of the cross-shore distance (x) and frequency (f). The black dashed lines represents $0.5f_p$, f_p and $1.5f_p$.

Simulations follow the settings described in Section 3.1, with a sponge layer at 7 m to prevent reflection at the back boundary. Second-order waves are generated offshore using a JONSWAP spectrum, and each run lasts 1,700 waves to be able to obtain reliable estimates for several wave parameters. A uniform spatial output resolution of $\Delta x = 0.5$ m is used for foreshore slopes A and B, $\Delta x = 0.25$ m for slopes C and D, and $\Delta x = 0.2$ m for slopes E and F, as steeper slopes were found to require a finer resolution to accurately estimate $S_{nl,HH}$. Time series (0.01 Hz) are analyzed after a 750 s spin-up time using Welch's method (50% overlap, sample length 4,000). This longer spin-up time is required to obtain a stationary time series for the spectral analysis, where any reflections from the foreshore are included. Only data from depths smaller than 0.8 m considered for visualization purposes.

First, results of the energy balance from a single test are presented, followed by a non-dimensional comparison of all simulations (Section 4.2). Lastly, the effect on the wave parameters is described (Section 4.3).

4.1. Energy Transfer

Figure 7 presents the wave spectrum, energy flux gradient (F_x), and nonlinear energy transfer ($S_{nl,f}$) for a simulation with $H_{m0} = 0.15$ m, $s_0 = 0.01$ and $m = 0.01$ using the Boussinesq formulation, showing that the distribution of the energy density varies within the domain. To quantify spectral energy transfer, frequency-integrated terms for the low-frequency (LF), primary (p), and high harmonics (HH) ranges are shown in Figure 8. The residual ($S_{nl,f} + F_{x,f}$), shown in gray, indicates dissipation of energy or limitations in the formulation due to the validity.

Considering the energy at frequencies higher than $1.5f_p$, second-order peaks arise in the wave spectrum at two times the peak frequency around $x = 0$ m (Panel b in Figure 7). The gradient in energy flux (Panel c in Figure 7)

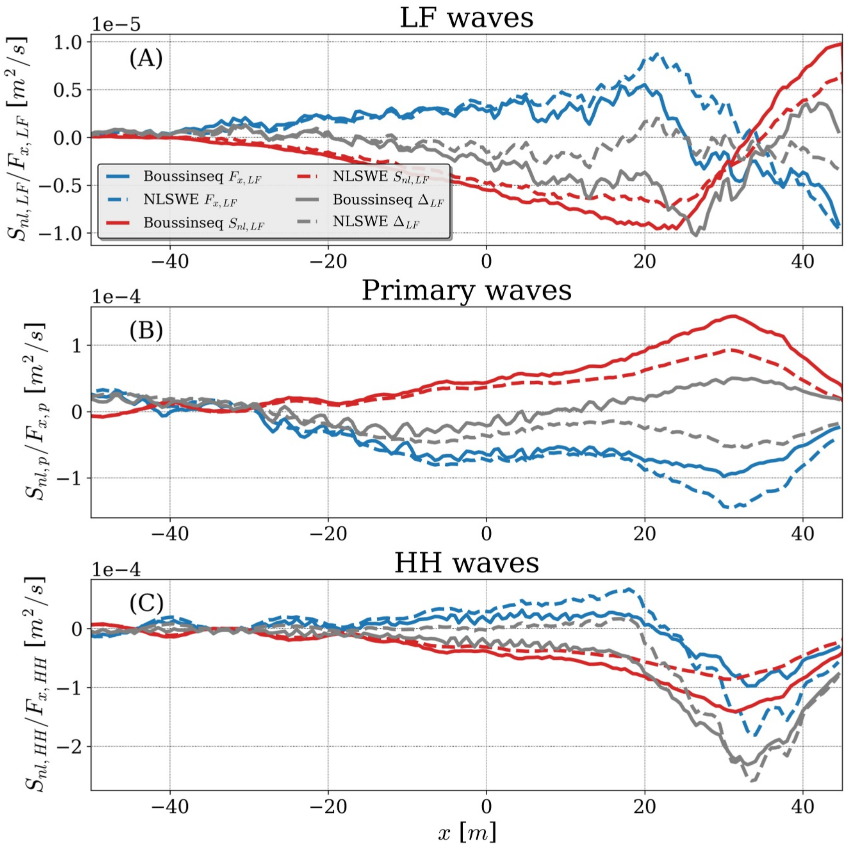

Figure 8. Summed gradient in energy flux ($F_{x,f}$), nonlinear energy transfer ($S_{nl,f}$) and balance residual (Δ_f) for the low-frequency components (LF, Panel a), primary components (p, Panel b) and higher harmonics (HH, Panel c) frequencies as a function of the cross-shore distance. Both the results computed with the Boussinesq formulation (Equations 10 and 11) and NLSWE (Equations 12 and 13) are shown. Results are shown for test with $H_{m0} = 0.15m$, $s_0 = 0.01$ and $m = 0.01$.

shows that most of the energy is transferred to these higher frequencies between $x \approx 0$ m and $x \approx 15$ m with a positive gradient in energy flux and a negative $S_{nl,f}$ around $f \approx 0.6Hz$. This energy is coming from energy around the peak, where the gradient in the energy flux is negative but the nonlinear source term is positive. From $x = 20$ m, $F_{x,f}$ becomes negative at $f \approx 0.6Hz$ and $S_{nl,f}$ turns positive, suggesting energy is transferred to even higher frequencies. Panel c of Figure 8 shows that the bulk integrated terms, including the residual, indicate an approximately closed balance in the shoaling zone. However, in the surf zone ($x > 20$ m), the balance becomes nonzero at higher frequencies, suggesting the presence of dissipation. Near the boundary, fluctuations in $F_{x,f}$ and $S_{nl,f}$ are observed most likely caused by the boundary as also observed in Figure 6.

Low-frequency energy appears near $x = 0$ m at $f_p/2$, transferred from the peak frequency region (negative $S_{nl,f}$ at $f < f_p/2$). From $x = 40$ m, this energy transfer decreases, indicated by a negative $F_{x,f}$, while $S_{nl,f}$ becomes positive, showing energy transfer back to higher frequencies. In Panel a of Figure 8, this is reflected in the bulk energy balance with a change of sign of $S_{nl,LF}$ around $x = 30$ m.

To verify whether the energy balance closes, the residual for three integrated frequency ranges is shown in Figure 8. The balance does not close perfectly across the entire domain, indicating either energy dissipation or limitations in the theoretical formulation. In the shoaling zone, where the Boussinesq model is valid, the residual is relatively small for the primary frequencies (Panel b in Figure 8). The nonlinear shallow water balance (NLSWE) shows slightly larger discrepancies due to the absence of dispersive effects and incomplete representation of shoaling. On the other hand, the NLSWE formulations show better results for the LF and HH components, especially in the surf zone where the Boussinesq theory shows larger residuals. The assumptions in the NLSWE balance are valid for the LF components but not necessarily valid for the HH components, but it is expected that dispersive effects are less important in shallow water compared to nonlinear effects. Overall, both

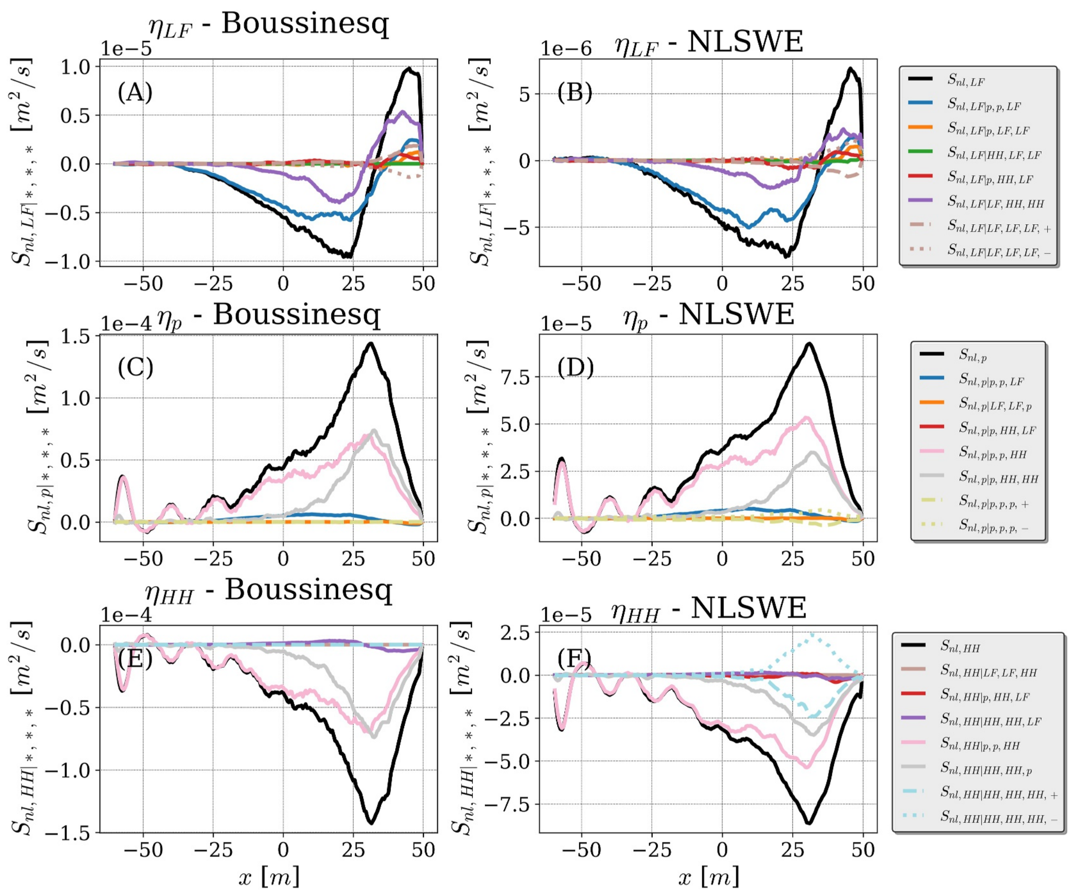

Figure 9. Nonlinear energy transfer, integrated over three frequency bands (low-frequency components, LF, in the Panels (a) and (b); primary components, p, in Panels (c) and (d); and higher harmonics, HH, in Panels (e and f), as a function of cross-shore location. The left panels (a, c, and e) show the result from Boussinesq's theory and the right panels (b, d, and f) shows the result from NLSWE. Results are shown for test with $H_{m0} = 0.15m$, $s_0 = 0.01$ and $m = 0.01$.

theories show similar behavior, allowing to identify the importance of the nonlinear energy transfer in the cross-shore direction, even though the values may contain some inaccuracies.

Figure 9 shows the contributions of the nonlinear energy transfer (S_{nl}) for various wave combinations of interactions, summed over three frequency ranges (LF in upper panels, p in middle panels and HH in the lower panels). Next to the energy transfer between the various frequency bands, also the energy transfer within a frequency band, which integrates to zero over the frequency band, is shown as the positive and negative contributions (e.g., $S_{nl,LF|LF,LF,LF,\pm}$). The left panels show the results for the Boussinesq formulation, and the right panels show the results for the NLSWE formulation.

In the shoaling zone ($x < 25$ m), most of the energy is transferred by a triad involving two primary components and either one LF component ($S_{nl,LF|p,p,LF}$) or one HH component ($S_{nl,HH|p,p,HH}$). For this particular test, most energy is going to higher frequencies as $S_{nl,HH|p,p,HH}$ is an order of magnitude larger than $S_{nl,LF|p,p,LF}$. From $x \approx 0$ m, additional triad combinations become significant as well. For the low-frequency range (Panels a and b in Figure 9), interactions between two high-frequency components and one low-frequency component ($S_{nl,LF|HH,HH,LF}$) contribute to the energy transfer. Also deep in the surf zone ($x > 27$ m), the energy transfer within the LF region becomes important with larger $S_{nl,LF|LF,LF,LF,+}$ balanced by $S_{nl,LF|LF,LF,LF,-}$ resulting in a nonlinear LF wave shape. In very shallow water, the $S_{nl,LF|p,LF,LF}$ interaction accounts for energy transfer to higher frequencies but this is very limited. The interactions $S_{nl,LF|HH,LF,LF}$ and $S_{nl,LF|p,LF,HH}$ do not show significant energy transfer for this test.

For high-frequency components (Panels e and f), a triad involving two primary waves and one HH wave accounts for a substantial portion of the energy transfer ($S_{nl,HH|p,p,HH}$). From $x \approx 25$ m, the interaction with two HH components and one primary component also becomes dominant ($S_{nl,p|p,HH,HH}$). The $S_{nl,p|p,HH,HH}$ interaction likely involves components at the peak frequency, the first higher harmonic, and the second higher harmonic (see also Appendix A). In contrast to the low-frequencies, the S_{nl} remains negative for the high frequencies, showing that energy is only going from the primary components to the higher frequencies.

The Boussinesq and NLSWE balances show very similar results for the low-frequencies, but for the higher frequencies, larger differences occur. For example, the $S_{nl,p|p,HH,HH}$ becomes larger than $S_{nl,p|p,p,HH}$ for the Boussinesq formulation, whereas the NLSWE shows the opposite. However, in the HH frequency range (Panels e and f) $S_{nl,p|p,p,HH}$ is always dominant for both formulations. A second difference is the energy transfer within the HH frequency range ($S_{nl,HH|HH,HH,HH,+}$), which is significantly larger for the NLSWE than for the Boussinesq formulation. It is argued that the NLSWE balance is preferred for both the higher harmonics and low-frequencies in the surf zone as the found residuals in the energy balance or lower and mainly nonlinear effects are important.

4.2. Non-Dimensional Overview

To show how the different interactions vary for the wave conditions, the nonlinear energy transfer is normalized. To compare various simulations, the results are normalized with $H_{m0}^2 \Delta f$, and to show the contribution of a specific interactions, it is normalized by the total nonlinear energy transfer in a specific frequency band (LF, primary or HH). As several interactions occur in the same frequency range for irregular waves, it is impossible to identify precisely where the energy at a specific frequency is coming from. Therefore, only bulk parameter properties over a frequency range can be studied. To demonstrate how the interactions change the spectral shape, in Appendix A, the results are also shown for a bichromatic wave for which it is possible to show the interactions in more detail. In addition, the effects of the interactions are illustrated using the bicoherence and biphase of the corresponding interaction.

The NLSWE formulation is applied for the LF and HH components, and the Boussinesq formulation is applied for the primary components. This division results in the lowest balance residual as dispersive effects are not ignored for the primary waves and nonlinear effects are included for both the LF and HH components.

The results are presented as functions of relative depth (kh, representing water depth, where k is computed given the offshore peak period), offshore wave steepness ($s_{m-1,0,\text{deep}}$, representing nonlinearity), and the normalized slope or Iribarren number $\xi = m/\sqrt{s_{m-1,0,\text{deep}}}$ (Battjes, 1974), which represents the foreshore slope. A summary of the findings is provided in Table 4, distinguishing between deep- and shallow-water conditions, low and high wave steepness, and mild and steep normalized slopes. These observations are discussed in more detail in the following sections.

4.2.1. Energy Balance

The frequency summed terms over the three defined frequency ranges are shown in Figure 10. As kh decreases, energy transfer to HH and LF components increases with more energy transfer for steeper waves for the same kh (Panels a–c in Figure 10). For mild sloping profiles ($\xi < 0.2$), both positive and negative energy flux occur for the low frequencies balanced by the nonlinear energy transfer for the three wave steepnesses (Panels a and d in Figure 10). Thus, LF frequencies receive energy in the shoaling zone, and transfer energy back to higher frequencies in the surf zone. For steeper foreshore slopes ($\xi \geq 0.2$), the low-frequency components only receive energy. For mild sloping profiles, the maximum normalized energy transfer is positive in very shallow water, whereas the maximum for steep foreshore slopes is negative. As the energy flux and nonlinear energy transfer have opposite signs, the balance closes with a relative error of maximum 4% of the total energy (Panel g in Figure 10).

For the primary components, there is mainly a negative energy flux, showing that these frequencies only lose energy. Conditions with high offshore wave steepness result in a higher energy transfer to other frequencies (Panel e in Figure 10), where the conditions with a steep foreshore slope show the largest energy transfer. The error in the balance is larger with an error up to 50% of the total energy, but this large error is mainly found in

Table 4
Overview of Numerical Results for Energy Transfer ($S_{nl,*,*,*}$) and Biphase ($\phi_{*,*,*}$)

	$\xi < 0.2$		$\xi > 0.2$	
	Low s	High s	Low s	High s
Energy transfer relevant for LF energy				
Shallow	$S_{nl,p,p,LF} \geq 0$		$S_{nl,p,p,LF} < 0$	
Shallow	$S_{nl,p,p,LF} \approx 50\% S_{nl,LF}$ and $S_{nl,HH,HH,LF} \approx 50\% S_{nl,LF}$			
Deep	$S_{nl,p,p,LF} \approx 100\% S_{nl,LF}$			
Shallow	$S_{nl,p,LF,LF} > 0$	$S_{nl,p,LF,LF} < 0$	$S_{nl,p,LF,LF} \approx 0$	
Biphase	$\phi_{p,p,LF}: 180° \rightarrow -50°$		$\phi_{p,p,LF}: 180° \rightarrow 90–180°$	
Redistribution of LF energy				
Shallow	$S_{nl,LF,LF,LF} \neq 0$		$S_{nl,LF,LF,LF} \approx 0$	
Biphase	$\phi_{LF,LF,LF}: 180° \rightarrow 90°$		$\phi_{LF,LF,LF}: 180° \rightarrow 90°$	
Energy transfer relevant for HH energy				
Shallow	$S_{p,p,HH} \approx 50\% S_{nl,HF}$ and $S_{p,HH,HH} \approx 50\% S_{nl,HF}$			
Deep	$S_{nl,p,p,HH} \approx 100\% S_{nl,HF}$			
Biphase	$\phi_{p,p,HH}$ and $\phi_{p,HH,HH}$ shift toward $-90°$ with increasing ξ			
Redistribution of HH energy				
Shallow	$S_{nl,HH,HH,HH} \approx 0$		$S_{nl,HH,HH,HH} > 0$	
Biphase	$\phi_{HH,HH,HH}$ shifts toward $-90°$ with increasing ξ			

Note. The parameter s represents $s_{m-1,0,\text{deep}}$, with a threshold at 0.02.

relatively deep water. The cause of the larger error in deep water remains unclear, but it appears from a nonzero energy flux in deep water.

The high frequency region is the only region of the spectrum where the energy flux does not balance the nonlinear energy transfer at all (Panels c, f, and i in Figure 10). In the shoaling zone, the HH components receive energy (positive flux) and in the surf zone, these components lose energy. These patterns are not significantly different for the various foreshore slopes (Panel c in Figure 10). The gain of energy is the largest for the low steepness conditions. The energy transfer is only negative, which indicates that these frequencies receive energy for all values of kh (Panel f in Figure 10). The largest relative energy transfer is observed for steeper foreshore slopes (Panel f in Figure 10). The combination of a negative energy flux and negative nonlinear energy transfer in the surf zone indicates energy dissipation (balance does not close). The largest energy balance residual is found for the steeper foreshore slopes, which can be explained by the fact that there is a lot of energy dissipation over a short distance, whereas the energy at the milder foreshore slopes dissipates over a longer distance.

4.2.2. Energy Transfer Lower Frequencies

The interactions affecting the low-frequency components are discussed first (see Figure 11). Two interactions mainly contribute to the transfer of energy toward the LF band. In relatively deep water, $S_{p,p,LF}$ is the dominant contribution, whereas in shallow water $S_{HH,HH,LF}$ also becomes important. In the surf zone, both interactions contribute approximately equally, each accounting for about 50% of the total transfer (see Panels b and f). In contrast, in deep water $S_{p,p,LF}$ accounts for nearly all of the LF energy transfer (see Panel b). Because the interaction signs vary with depth, the normalized transfer shows increased scatter, especially when the normalization factor is small.

Normalized foreshore slope mainly affects the sign of the transfer. Steeper slopes ($\xi \geq 0.2$) produce consistently negative values, indicating LF energy gain, whereas mild slopes show LF energy loss in the surf zone for both $S_{nl,p,p,LF}$ and $S_{nl,HH,HH,LF}$.

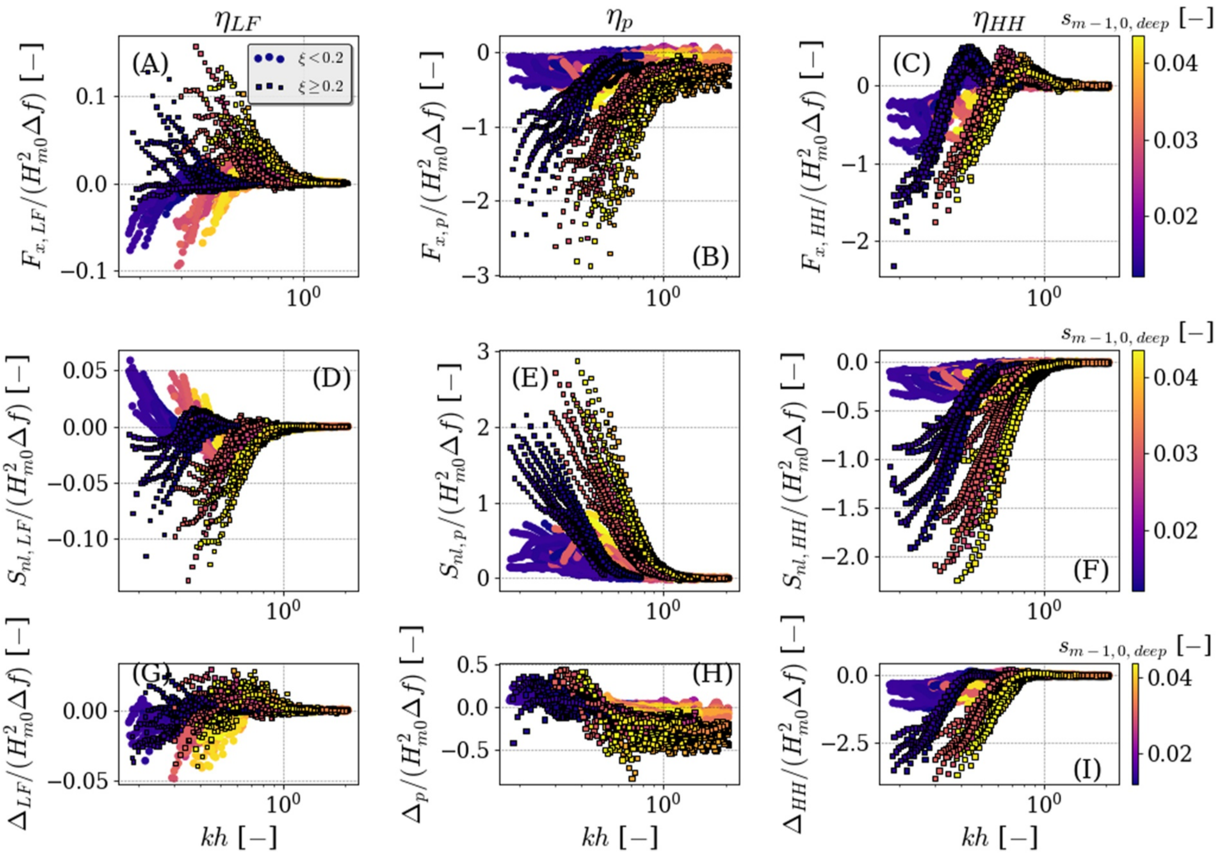

Figure 10. Energy flux (Panels a–c), nonlinear energy transfer (Panels d–f) and balance residuals (Panels g–i) for the low-frequency (LF), primary (p) and higher harmonic (HH) components (left, middle and right panels). NLSWE is used for the LF and HH components, and Boussinesq theory is used for the primary waves. For the LF and HH components, results are only shown for $H_{m0,LF}/H_{m0} > 0.05$ or $H_{m0,HH}/H_{m0} > 0.05$ to prevent division by a small number.

The significance of these interactions is further illustrated by the bicoherence terms $B_{p,p,LF}$ and $B_{HH,HH,LF}$. The bicoherence $B_{p,p,LF}$ is relatively high at the offshore boundary and increases toward the breaking point, beyond which it decreases. In deep water, the LF components are approximately out of phase with the primary components (≈180°, Panel d). After breaking, the correlation weakens and the LF components propagate as free waves, resulting in lower bicoherence values. In the surf zone, it increases again as the high frequency waves can only exist on top of the low-frequency crest. Mild slopes show a biphase transition from 180° to −50° for both $\phi_{p,p,LF}$ and $\phi_{HH,HH,LF}$, whereas steeper slopes result in values closer to 180°.

In addition to triads involving a single LF component, energy can be transferred to higher frequencies through $S_{nl,p,LF,LF}$ or redistributed within the LF band by $S_{nl,LF,LF,LF}$ (Figure 12). The term $S_{nl,LF,LF,LF}$ is only relevant for mild foreshore slopes (Panels a and b). Although its absolute magnitude is small (Panel a), it can contribute up to roughly 30% of $S_{nl,LF}$ within the LF band (Panel b, ignoring scatter).

A similar pattern occurs for $S_{nl,p,LF,LF}$, which is negligible for steep slopes but becomes nonzero for milder ones. For steep offshore conditions, the transfer is initially negative and turns positive further into the surf zone, while mild conditions show consistently positive values of larger magnitude.

These trends are reflected in the bicoherence and biphase. The bicoherence $B_{LF,LF,LF}$ increases through the shoaling zone and decreases after breaking, with the highest values under low-steepness conditions. The associated biphase changes from approximately −180° to about −50°. Energy transfer toward higher frequencies through triads involving two LF components and one primary component is captured by $B_{p,LF,LF}$. This interaction is only relevant in very shallow water and occurs primarily for mild slopes under low wave steepness.

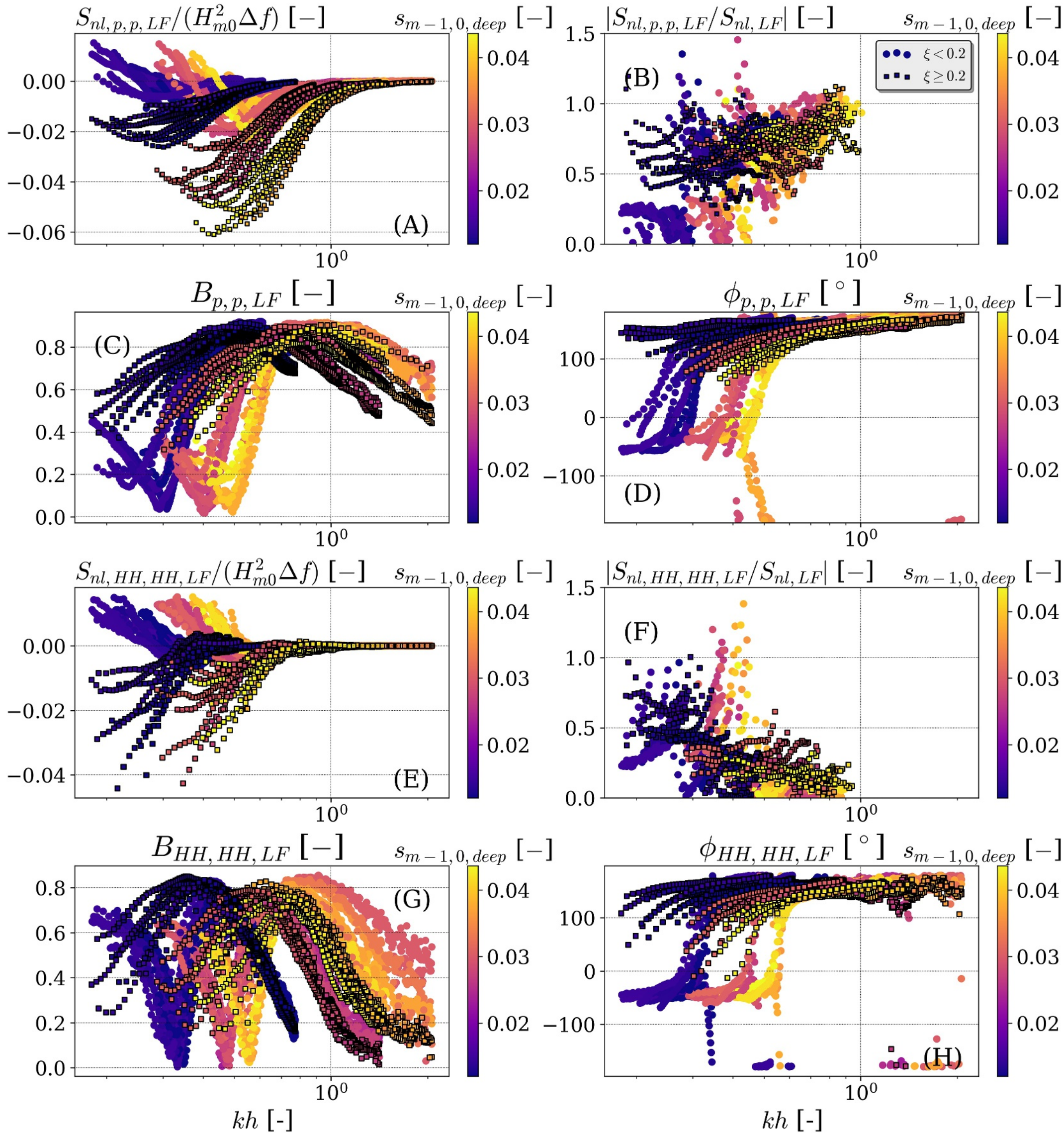

Figure 11. Nonlinear interactions ($S_{nl,*,*,*}$) between low-frequency (LF), primary (p), and higher-harmonic (HH) components associated with the low-frequency range, shown as a function of relative water depth (kh). Results are presented using two normalizations: $H_{m0}\Delta f$ (Panels a and e) and $S_{nl,LF}$ (Panels b and f). The corresponding bicoherence and biphase are shown in Panels (c, d, g, and h). Results are omitted when $S_{nl,LF}/(H_{m0}\Delta f) < 0.05$.

4.2.3. Energy Transfer Higher Harmonics

The transfer of energy toward higher frequencies is primarily governed by the triad involving two primary components and one higher-harmonic (HH) component (Panels a and b in Figure 13). This interaction accounts for nearly 100% of the energy transfer for $kh > 0.5$. In shallower water ($kh < 0.5$), the triad consisting of two HH components and one primary component also becomes significant, contributing approximately 50% of the total transfer (Panel f in Figure 13). This contribution is most likely associated with interactions between the spectral peak (f_p), the first higher harmonic $(2f_p)$, and the second higher harmonic $(3f_p)$.

For all conditions considered, the HH components receive energy, as indicated by the negative sign of the nonlinear energy transfer. When normalized by the local wave height, steeper foreshore slopes result in a relatively larger transfer of energy to higher frequencies compared to milder slopes (Panels a in Figure 13).

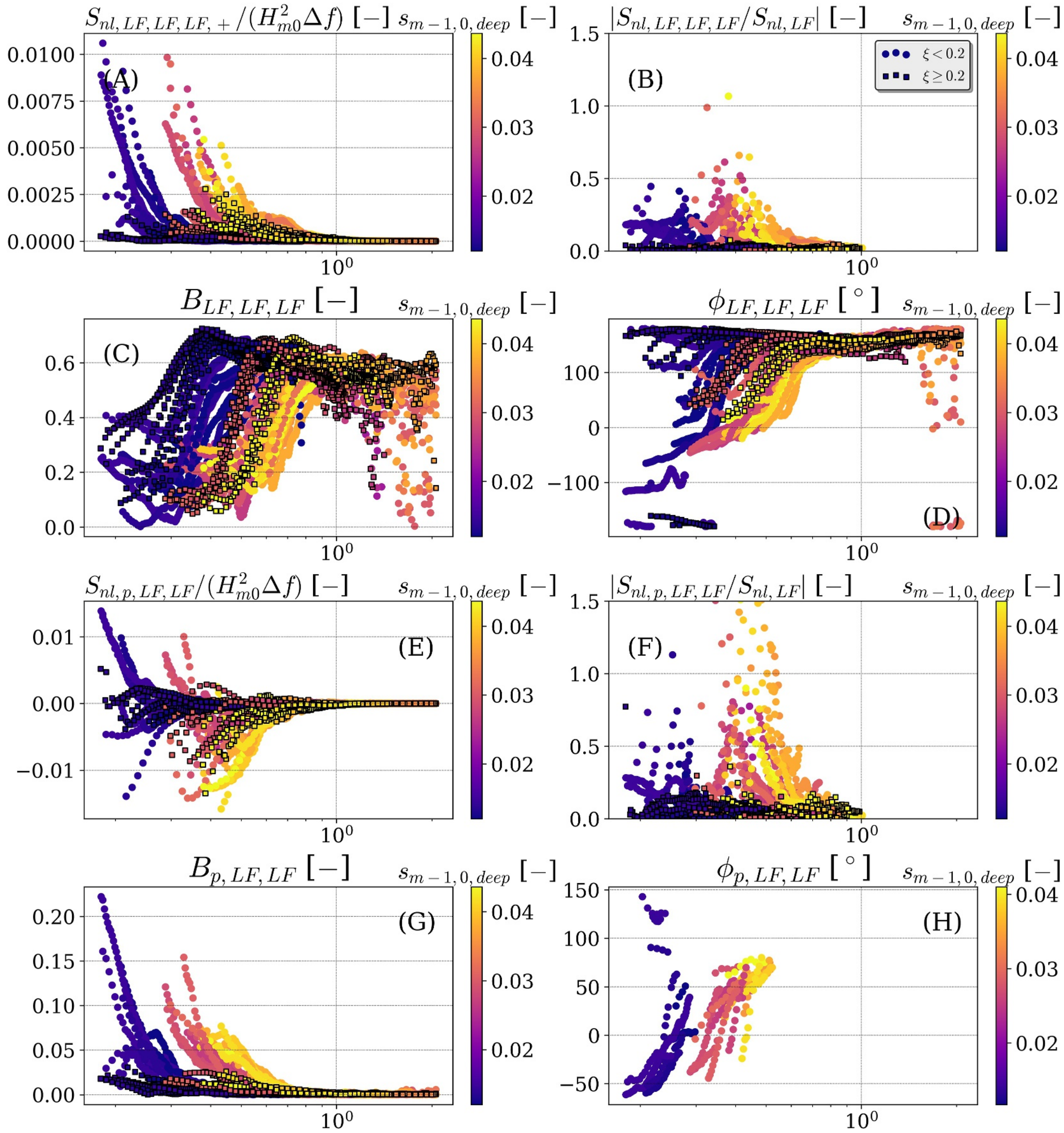

Figure 12. Nonlinear interactions ($S_{nl,*,*,*}$) between low-frequency (LF), primary (p), and higher-harmonic (HH) components influencing η_{LF}, shown as a function of relative water depth (kh). Results are presented using two normalizations: $H_{m0}\Delta f$ (Panels a and e) and $S_{nl,LF}$ (Panels b and f). The corresponding bicoherence and biphase are shown in Panels (c, d, g, and h). Results are omitted when $S_{nl,LF}/(H_{m0}\Delta f) < 0.05$.

The energy transfer to higher harmonics depends on both the foreshore slope and the offshore wave conditions. The bicoherence of the triad involving one higher harmonic, $B_{p,p,HH}$ (Panel c of Figure 13), is larger for higher wave steepnesses, while the associated wave shape is influenced by the foreshore slope (Panel d). In deep water, the biphase is close to zero, corresponding to skewed wave shapes. In shallow water, the biphase shifts toward approximately $-90°$, indicating increasingly asymmetric waves, with steeper foreshore slopes yielding lower biphase values than milder slopes.

The maximum bicoherence of $B_{p,p,HH}$ occurs at approximately the same relative depth as that of $B_{p,p,LF}$, just prior to breaking. Similar behavior is observed for $\phi_{p,HH,HH}$, for which the foreshore slope has a comparable influence. However, in this case the correlation is significantly weaker in deep water compared to the $\eta_p\eta_p\eta_{HH}$ interaction.

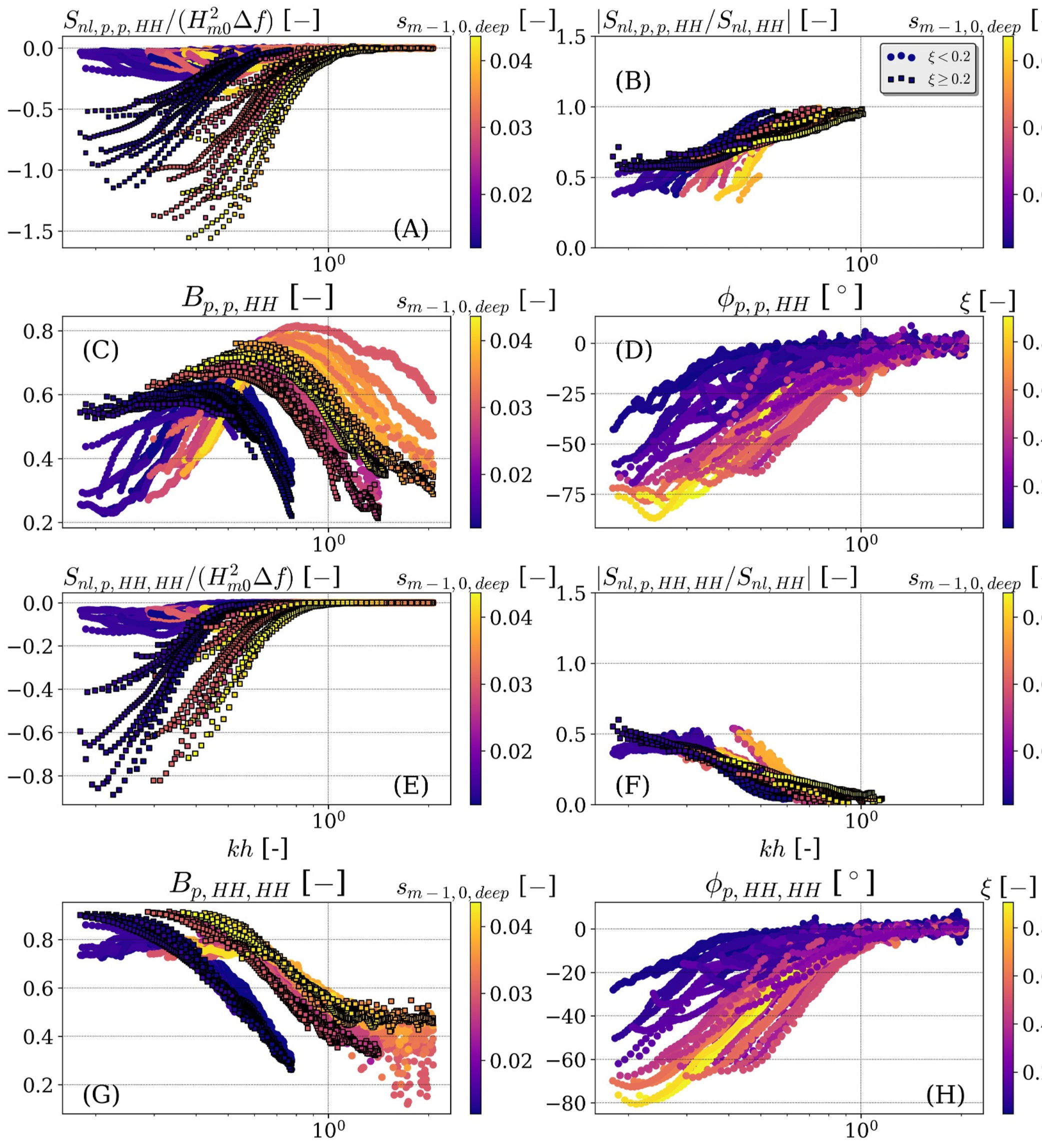

Figure 13. Nonlinear interactions ($S_{nl,*,*,*}$) between low-frequency (LF), primary (p), and higher-harmonic (HH) components associated with the higher harmonics, shown as a function of relative water depth (kh). Results are presented using two normalizations: $H_{m0}\Delta f$ (Panels a and e) and $S_{nl,LF}$ (Panels b and f). The corresponding bicoherence and biphase are shown in Panels (c, d, g, and h). Results are omitted when $S_{nl,LF}/(H_{m0}\Delta f) < 0.05$.

Thus, steeper foreshore slopes ($\xi > 0.2$) result in significantly more energy transfer toward higher harmonics than milder slopes. In deep water this transfer is dominated by $S_{nl,p,p,HH}$, while in shallow water $S_{nl,p,HH,HH}$ also contributes. The biphase of this triad strongly depends on the foreshore slope.

The redistribution of energy within the HH region is shown in Figure 14. Also here, as kh decreases, the energy transfer within the HH band becomes stronger, indicated with the positive contribution of this interaction (Panel a). This interaction becomes 50% of the total interaction in this frequency range in shallow water (Panel b). Normalized by the total nonlinear energy transfer, the results are very similar, but larger variations are observed when normalized with the wave height (Panel a in Figure 14), where the interaction is stronger for steeper foreshore slopes. Note that this interaction is not part of $S_{nl,LF}$ as it integrates to zero in this frequency range.

The wave shape of the higher harmonics, represented by $B_{HH,HH,HH}$, becomes relevant only in shallow water ($kh < 1$). For steeper wave conditions, the bicoherence reaches its maximum at larger relative depths compared

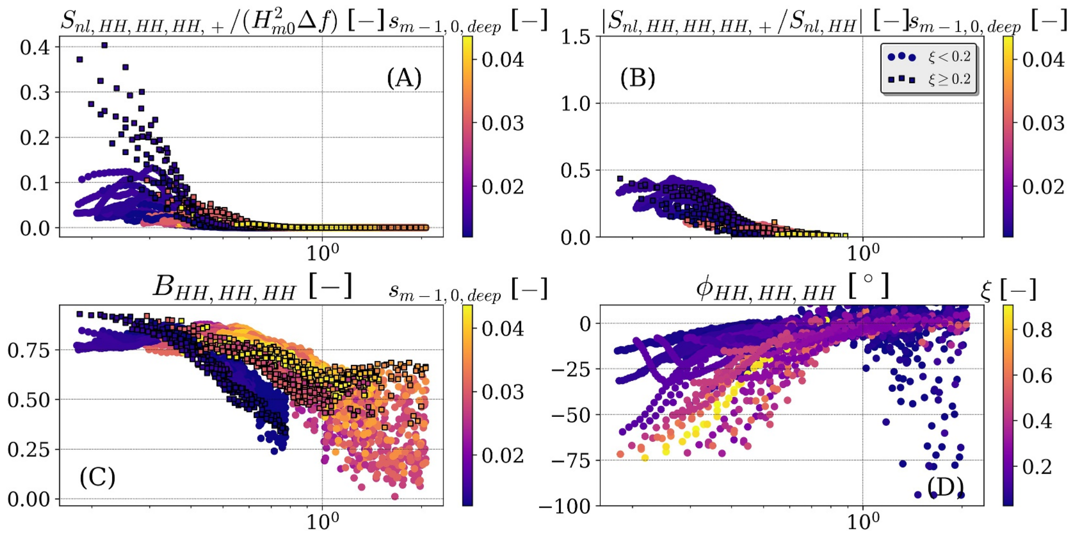

Figure 14. Nonlinear interactions ($S_{nl,*,*,*}$) between low-frequency (LF), primary (p), and higher-harmonic (HH) components associated with the higher harmonics, shown as a function of relative water depth (kh). Results are presented using two normalizations: $H_{m0}\Delta f$ (Panels a) and $S_{nl,LF}$ (Panels b). The corresponding bicoherence and biphase are shown in Panels (c) and (d). Results are omitted when $S_{nl,LF}/(H_{m0}\Delta f) < 0.05$.

to low–steepness conditions (Panel g). In very shallow water ($kh < 0.5$), the bicoherence remains relatively constant for all conditions.

The biphase shifts from approximately 0° toward −90° depending on the foreshore slope, indicating increasingly asymmetric HH wave shapes in shallow water. This asymmetry is more pronounced for steeper foreshore slopes.

4.2.4. Effect Slope

To demonstrate the effect of the normalized slope, the biphase of the dominant interactions is shown in Figure 15 as a function of $kh^{-1}s_{m-1,0}^{0.5}$ for profiles A, B, C, D, E, and F. Using $kh^{-1}s_{m-1,0}^{0.5}$ on the x-axis accounts for the influence of wave steepness. Other non-dimensional parameters (e.g., U_r) were also examined, but they did not yield noticeably better relationships.

These results show that the normalized slope influences the biphase of the various interactions. For the low frequencies, steeper slopes yield a more constant value for $\phi_{p,p,LF}$, $\phi_{LF,LF,LF}$, and $\phi_{HH,HH,LF}$, whereas milder slopes show a transition of the biphase toward −50°. Visual inspection indicates that this transition consistently occurs for $\xi < 0.2$, while steeper slopes show greater variability as a function of ξ. This implies that in shallow water, the primary and higher harmonics predominantly occur on top of the LF crest, whereas for steeper slopes this effect becomes less pronounced.

For the higher harmonics, ξ affects $\phi_{p,p,HH}$, $\phi_{HH,HH,HH}$, and $\phi_{p,HH,HH}$. Here, no clear transition is observed. Instead, the biphase gradually decreases in shallow water for steeper slopes. More energy is transferred to higher harmonics under steeper-slope conditions, resulting in increased energy at these harmonics and therefore smaller values of ϕ. Because energy is also transferred to components at frequencies higher than $2f_p$, $\phi_{p,HH,HH}$ is likewise influenced by ξ. Thus, for $\xi \approx 0.2$, a transition is observed in the low-frequency biphases, while the higher frequencies show a more gradual behavior.

4.3. Wave Parameters

The energy transfer between frequencies affects how the energy is distributed while propagating over the foreshore. In Figure 16, the effect of this redistribution of energy and dissipation of energy is shown for the wave height computed over several frequency bands ($H_{m0,LF}$, $H_{m0,p}$ and $H_{m0,HH}$). To distinguish between the relative and absolute change of energy, the wave heights are normalized with the offshore wave height (e.g., $H_{m0,LF}/H_{m0,\mathrm{deep}}$, left Panels) and the local wave height (e.g., $H_{m0,LF}/H_{m0}$, right panels). Also, note that

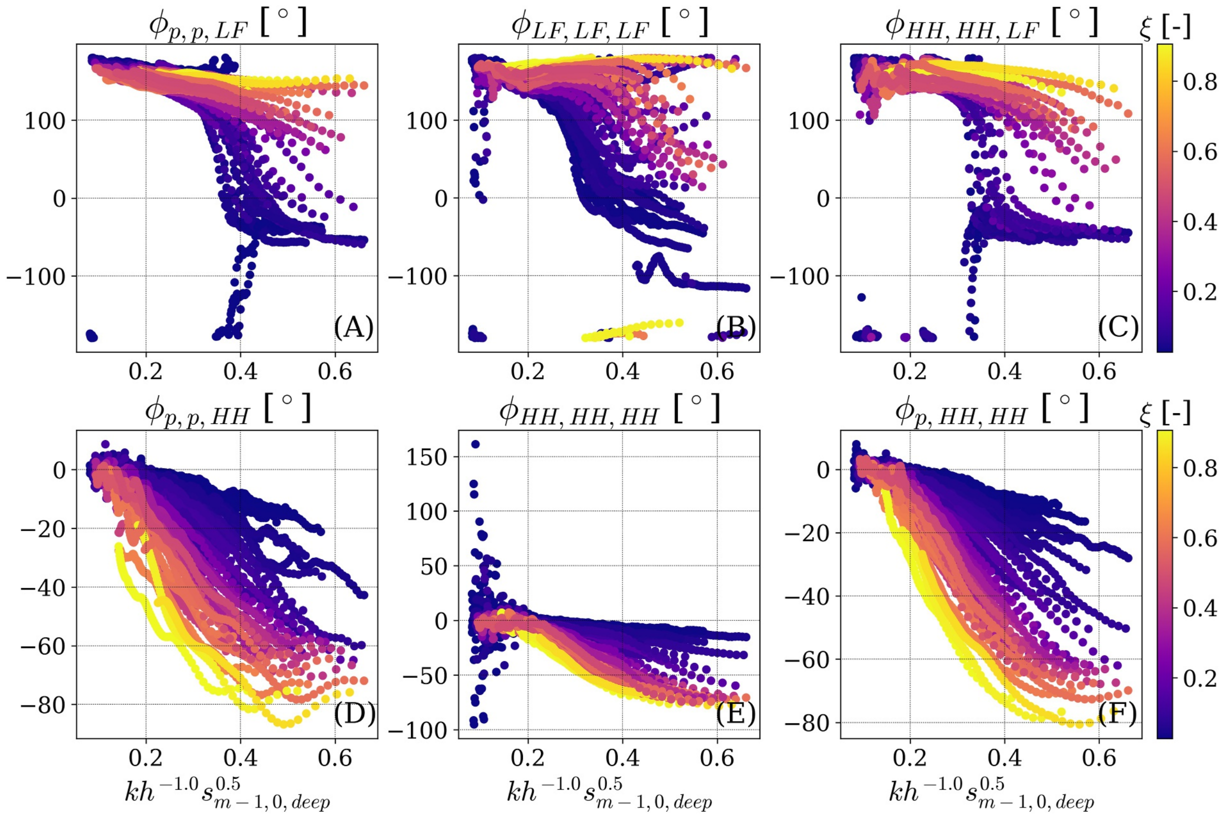

Figure 15. Biphase $(\phi_{*,*,*})$ as function of $kh^{-1}s^{0.5}_{m-1,0,\mathrm{deep}}$ for various signals where the color represent the normalized slope $\left(\xi = m/\sqrt{s_{m-1,0,\mathrm{deep}}}\right)$ for profiles A, B, C, D, E, and F. Panel (a) shows the biphase of two primary components and one low-frequency waves, Panel (b), the biphase of the low-frequency components, Panel (c), the biphase of two higher harmonics and one low-frequency component, Panel (d) the biphase for two primary waves and one higher harmonic, Panel (e) the biphase for the higher harmonics and Panel (f) the biphase of two higher harmonics and one primary wave.

energy is conserved and not the wave height itself, making the relative contribution of the wave height do not sum up to one. Moreover, as the frequency bands are correlated in shallow water, the energy of the three frequency bands does not necessarily have to sum up to the energy of the total signal.

In deep water ($kh > 1$), all the energy is located at the primary waves (Panels c and d in Figure 16). As the water depth decreases, energy is transferred to higher and lower frequencies. In absolute values, lower wave steepness conditions result in a larger energy transfer to higher components (Panel a in Figure 16), but the relative contribution does not show a large effect of the steepness (Panel b in Figure 16). The same behavior is observed for the various foreshore slopes, with a slightly lower energy transfer for the steeper foreshore slopes and the low steepness conditions (Panel b in Figure 16). The maximum of the energy at higher harmonics is located just before the breaking point and reduces again in the surf zone. This reduction matches the reduction of the total energy, as the reduction is not observed for the relative higher harmonic wave height in Panel b of Figure 16.

The energy transfer to the lower frequencies is dependent on the steepness (Panel f in Figure 16). For the same kh number, high wave steepness conditions gain energy earlier than the low steepness conditions. Moreover, the conditions with a mild foreshore slope result in significantly more energy ($H_{m0,LF}/H_{m0} = 0.6$) than the conditions with a steeper foreshore slope ($H_{m0,LF}/H_{m0} = 0.2$). In absolute values, the behavior is less clear, but it shows that the amount of energy varies between 15% and 30% of the total offshore wave height. After the breakpoint, the energy of the LF waves also reduces again. However, when the dissipation of the total wave height is taken into account, the relative contribution keeps growing (Panel f in Figure 16).

In the shoaling zone, the energy transfer results in a reduction in the primary frequency of the spectrum (Panel d of Figure 16). In deep water, almost all energy is located at the primary frequencies. In shallow water, the amount of energy in the primary frequencies decreases to $50-80\%$ depending on the foreshore slope or wave steepness. For

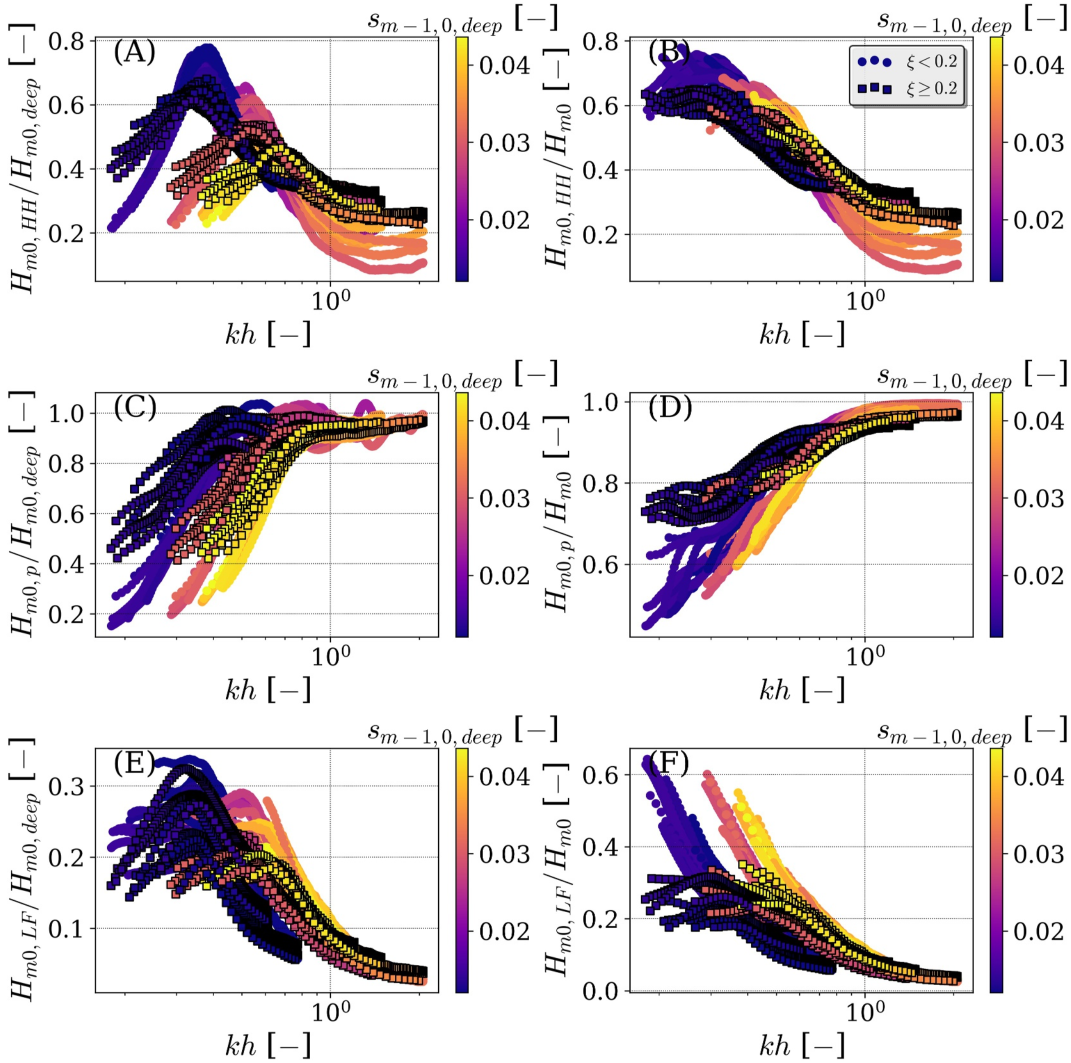

Figure 16. Absolute (left) and relative (right) wave height as a function of the relative depth (kh) for the low-frequency wave height (Panels a and b), wave height computed over the primary frequencies (Panels c and d) and the wave height computed over the higher frequencies (Panels e and f). Colors represent the deep-water wave steepness ($s_{m-1,0,\text{deep}}$).

the steeper foreshore slopes, the relative constriction of the energy at the primary frequencies is larger compared to the milder foreshore slopes (Panel d of Figure 16). Also, the absolute energy at the primary frequencies is larger for the steeper foreshore slopes compared to the milder foreshore slopes. As the energy growth at the LF and HH frequencies is not significantly different for the different foreshore slopes, this suggests that there is less wave dissipation at the primary frequencies for the steeper foreshore slopes.

The evolution of several wave parameters next to the wave height is shown in Figure 17. Since energy at lower frequencies strongly influences the spectral period ($T_{m-1,0}$), the parameters are computed based on a spectrum that excludes these lower frequencies (below $f_p/2$). This results in parameters representative of the high-frequency (HF) range, referred to as the HF frequency range.

In Panels a and b of Figure 17, the effect of the foreshore on the spectral period is shown by comparing the ratio of the HF spectral period ($T_{m-1,0,HF}$) with the deep water (left panels) and local total spectral period (right panels). It can be observed that the period becomes shorter when the water depth decreases by a factor of 0.7. In the shoaling zone, this is mainly caused by an increase in energy at higher frequencies. After the breakpoint, also the reduction of energy by dissipation (mainly at the peak) is an explanation for the reduction of the $T_{m-1,0,HF}$. When the HF

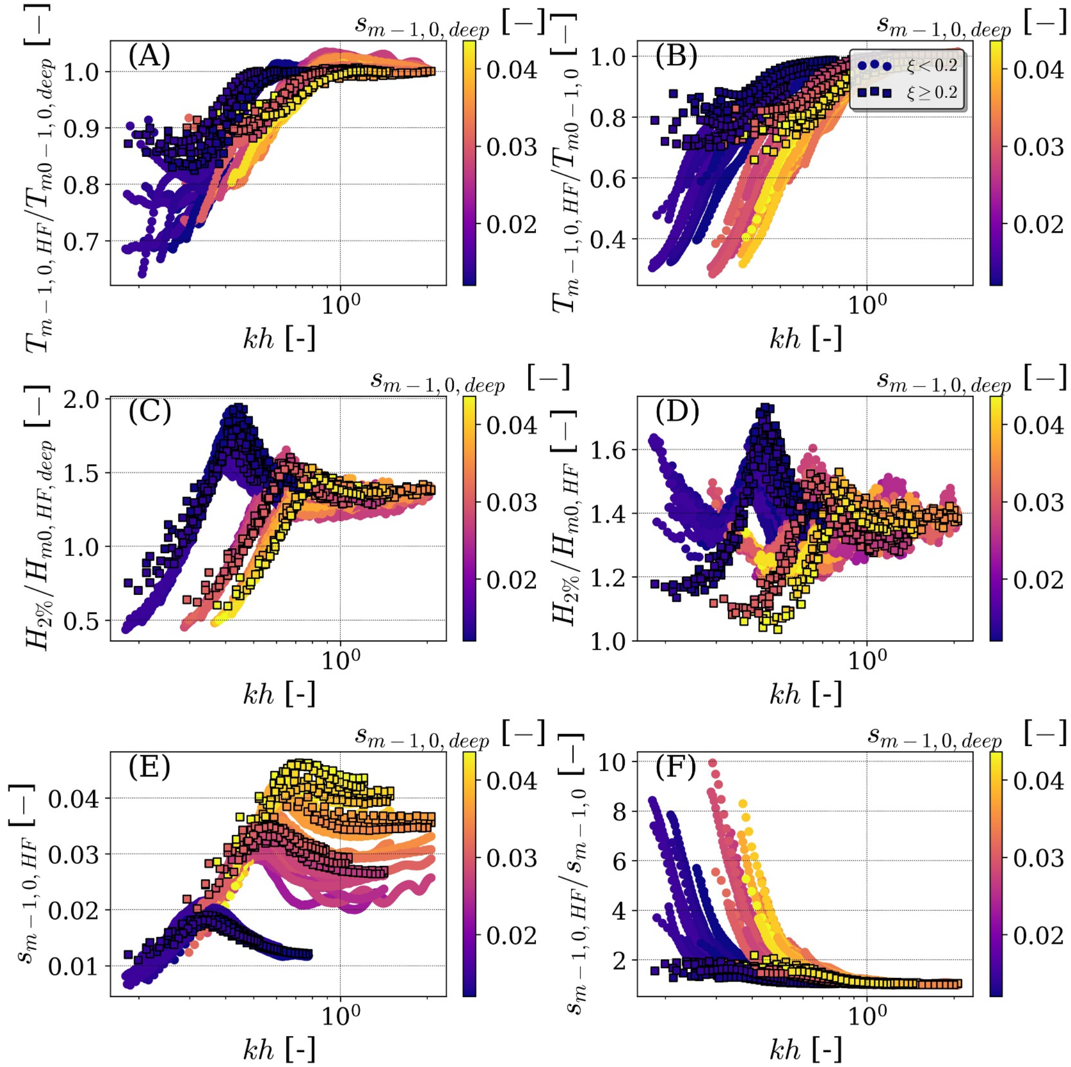

Figure 17. Spectral period (Panels a and b), 2% exceedance wave height (Panels c and d) and wave steepness (Panels e and f) as a function of the relative depth (kh). Colors represent the deep-water wave steepness ($s_{m-1,0,\mathrm{deep}}$). The left panels show the variables as a function of the deep water variable and the right panels as a function of the local spectral properties (local spectral period in Panel b, wave height in Panel d and steepness in Panel f).

period is compared to the total period, it can be seen that these two parameters diverge in shallow water. For mild sloping foreshore, the differences are very significant, but also for steeper foreshore slopes, the effect is visible.

The 2% exceedance wave height normalized with the deep water wave height (Panel c of Figure 17) shows similar results as the wave height with shoaling for the low steepness conditions up to the surf zone, and a reduction afterward. In the surf zone, only for the low steepness condition, an effect of the foreshore slope is observed with a slightly larger $H_{2\%}$. Following the Rayleigh distribution, the ratio between the $H_{2\%}$ and the HF wave height should be 1.4. In Panel d of Figure 17, this ratio is shown for the HF wave height $H_{m0,HF}$. In deep water, this relation is approximately 1.4, but changes significantly in shallow water, both depending on the foreshore slope and the steepness. Due to shoaling, the ratio increases up to almost 1.6 for the low steepness conditions. After the breaking point, the ratio decreases again due to wave breaking, but increases again for some conditions in very shallow water. Due to the energy at the low frequencies in very shallow water, the $H_{2\%}$ becomes relatively large compared to the wave height with an increase up to a factor 1.6 for the low steepness conditions.

In Panel e of Figure 17, the distribution of the wave steepness is shown, where the effect of wave breaking can be clearly observed. All three offshore wave steepnesses increase in the shoaling zone, especially for the low steepness condition, but all converge in the surf zone. Similarly, as has been shown for the spectral period, the frequency range over which the steepness is computed is very important in shallow water. The HF wave steepness can be 10 times larger than the steepness computed over the entire frequency range.

Thus, when all the wave parameters are compared, it can be seen that the distribution of energy can be significantly different, making it important to accurately simulate the nearshore conditions. Moreover, time domain parameters, like the 2% exceedance wave height, differ a lot because of the various wave shapes for different conditions, whereas the total energy over a certain frequency band is more consistent. To properly capture the wave steepness, it is important to distinguish between the higher frequencies and lower frequencies, especially for mild sloping profiles.

5. Discussion

This study examined the energy transfer across a wide range of wave conditions and profile slopes. The effects of profile variability are consistent with previous findings. Mildly sloping profiles produce nearshore conditions dominated by LF energy and steepening of the LF components, as also shown numerically by for example, De Bakker et al. (2016) and Rijnsdorp et al. (2022). The observed transformation of the biphase $\phi_{p,p,LF}$ agrees with earlier studies, with offshore values near 180° and nearshore values around −90° (Fiedler et al., 2019, De Bakker et al., 2015) or approximately −50° (Rijnsdorp et al., 2022). In the present analysis, the HH components are excluded from $\phi_{p,p,LF}$, which may lead to slight differences in absolute values, although the overall transition remains consistent with previous studies. Furthermore, Mendes et al. (2018) showed that energy is transferred back to higher frequencies for Ursell numbers exceeding 0.3–1, which is also observed here for mild foreshore slopes. However, this is not observed here for steep slopes showing the importance of a normalized slope (ξ). Fiedler et al. (2019) reported that offshore conditions have limited effect on the nearshore biphase, which aligns with the findings of this study for the $\phi_{p,p,LF}$. However, the present results demonstrate that variations in the normalized slope do influence the nearshore biphase.

Several studies have proposed non-dimensional slope parameters to describe LF behavior (e.g., Baldock, 2012; Battjes et al., 2004; Symonds et al., 1982; Van Dongeren et al., 2007). The present results show that the Iribarren number effectively captures the biphase transformation for both low and high frequencies with a transition in ξ for the low-frequencies and gradually dependency for the higher frequencies. Since most existing normalized bed slopes for LF waves are related to the Iribarren number, the results of this study are consistent with existing literature. For example, the non-dimensional slope proposed by Van Dongeren et al. (2007) is directly related to ξ, except that the steepness is based on the LF components. The different biphase behavior observed for steeper slopes suggests that the breakpoint-varying mechanism becomes dominant under these conditions as also found by Baldock (2012). This is also reflected in a higher reflection of LF energy (see Figure S1 in Supporting Information S1). The simulations indicate visually that this transition occurs at approximately $\xi \approx 0.2$. Using the normalized surf-zone width parameter χ proposed by Symonds et al. (1982), defined as

$$\chi = \left(\frac{\xi^*}{\sqrt{2\pi}}\right)^{-2}, \quad \text{with} \quad \xi^* = \frac{m}{\sqrt{h/L_{LF}}},$$

the transition value in terms of χ can be related to ξ. Based on the numerical results, a relationship $\xi^* \approx 5\,\xi$ is obtained. For a transition value of $\chi = 1.2$ (see Symonds et al., 1982), this yields $\xi \approx 0.45$ when the infragravity wavelength is estimated as $L_{LF} = g/(2\pi)T^2_{m-1,0,LF}$. This value exceeds the transition at $\xi \approx 0.2$ observed in the simulations. However, the discrepancy is likely a consequence of the uncertainty in the estimation of L_{LF}.

Considering the shape of the short waves, in the surf zone, Elgar and Guza (1985b) reported short-wave biphase values near −90°. Consistent with Rocha et al. (2017), the present results confirm that both foreshore slope and offshore steepness influence the biphase of the short-wave components which can vary between −90° and −20°.

Numerical results confirm that nearshore hydrodynamics are strongly influenced by both the geometry of the foreshore slope and the offshore wave conditions. Given that coastal defences are often situated in shallow water, the transformation of wave characteristics from deep to shallow regions is particularly relevant, as highlighted by previous studies (Lashley et al., 2021; Van Gent, 2001). When a shallow foreshore is a part of a coastal safety strategy, for example, as a climate adaptation measure (i.e., Van Gent, 2019), it is essential to assess its impact on nearshore dynamics. While such foreshores can effectively reduce wave heights in front of coastal defenses, they may also introduce unintended consequences. For instance, energy may be redistributed toward lower frequencies, potentially altering wave runup and overtopping behavior. Additionally, depending on ξ and offshore wave conditions, wave shapes may become increasingly nonlinear, with enhanced higher harmonics that further influence the interaction with the structure. This study has shown that these processes vary with foreshore geometry, offshore wave characteristics, and spatial location along the foreshore slope.

The validation of the two-layer non-hydrostatic model demonstrates its effectiveness and computational efficiency in capturing the nearshore wave dynamics, as also shown by other studies (i.e., Al Khalili et al., 2025; De Ridder et al., 2021; Den Bieman et al., 2024; Rijnsdorp et al., 2014; Smit et al., 2013, 2014; Suzuki et al., 2017). In contrast to phase-averaged models, the wave shape is accurately captured (See Figure 5), even with a simplified breaking formulation, showing its potential to estimate the nearshore wave conditions. Moreover, the model enables the use of time-domain parameters, such as $H_{2\%}$ or A_s, as parameters in the safety assessments of the sea defense, offering a more detailed representation compared to the bulk parameters typically derived from phase-averaged models.

The current findings are limited to conditions without significant directional spreading and assume normally incident waves, as the analysis is based solely on one-dimensional horizontal (1DH) simulations. It is well known that directional spreading affects the nearshore hydrodynamics, for instance by reducing low-frequency (LF) wave growth (i.e., Klopman & Dingemans, 2001). Additionally, obliquely incident waves will result in different behavior. Due to refraction, the wave growth in the shoaling of waves will be lower as refraction reduces the wave height. Also, here the effect of reflection was ignored by applying a sponge layer at the end of the domain. This approach will most likely match with most applications, where numerical simulations are performed without a reflective structure present and only incident waves propagate over the foreshore. It is therefore recommended to verify these findings also for directional sea states, including potential reflections from potential coastal obstacles.

In addition to potential reflections at the coastline, the foreshore slope also generates wave reflections as demonstrated by for example, Rijnsdorp et al. (2022). In our current approach, the biphase is computed from the total signal, which includes these reflections, as this will also be measured in the field. It is observed that for large values of ξ, a significant amount of low-frequency reflection occurs, which might also a potential cause for a mismatch in the energy balance (See Figure S1 in Supporting Information S1). Furthermore, the biphase computed based on the incident signal deviates from the current presented results based on the total signal, especially for steeper slopes. However, these deviations did not produce a completely different behavior and therefore the biphase on the total signal is shown, as the decomposition will also introduce an error.

The model uses a simplified breaking mechanism based on the steepness of free surface elevation (Smit et al., 2013). It can therefore be argued whether the energy transfer in the high-frequency part of the spectrum is accurately described, as overturning of waves and turbulent breakers are not modeled. However, the bicoherence and biphase, including high frequencies, are accurately reproduced as shown in the validation with the physical model experiments (see Figure 5), showing that the third-order statistics of the higher frequencies are accurately captured.

Furthermore, it seems that the NLSWE energy balance is more appropriate for the low and high frequencies, as the results are more consistent. However, as the truth energy transfer is not known, it is difficult to show which balance is more appropriate to apply outside or close to the applicability limits. For example, at steeper foreshore slopes, the assumption that changes in wave amplitude vary slowly is violated, and it is not known how this affects the accuracy of the energy transfer. Nevertheless, the consistency between the bicoherence, biphase and the energy transfer suggests that the found energy transfers are reliable, at least in demonstrating the relative importance of various energy transfers along the cross-shore profile. The balance is not always fully closed, which may be due to invalid assumptions, dissipation of energy or reflections. This also makes it difficult to explicitly demonstrate where in the spectrum energy is dissipated. While the results suggest that most of the energy is dissipated in the high-frequency tail, as also proposed by other authors (Bonneton, 2023; Herbers & Burton, 1997; Rijnsdorp et al., 2022), this cannot be proven using the current approach.

6. Conclusions

In this study the effect of the foreshore slope and offshore wave conditions on the nonlinear wave interactions across three frequency-integrated bands in shallow water are numerically studied.

Two types of non-hydrostatic wave models are validated using wave flume experiments to simulate wave hydrodynamics over sloping foreshores under severe wave breaking conditions (SWASH and XBeach). Three SWASH model setups are tested: one excluding low-frequency at the boundary, and two using either 2 or 10 vertical layers. Both bulk wave parameters, third-order statistics, and the energy transfer based on the Boussinesq formulation are verified. Across various offshore wave conditions and foreshore slopes, the models show high accuracy, with R^2 higher than 0.95 for the wave parameters. The differences between XBeach and SWASH are minor, except for the third-order statistics, where SWASH performs slightly better. Simulations excluding low-frequency waves at the boundary show reduced accuracy for the low-frequency wave height and wave shape of these lower frequencies. Sensitivity analysis reveals that at least two vertical layers are necessary to account for the right dispersive behavior and thereby accurately capture third-order statistics. Thus, SWASH is the preferred model in this study.

The two-layer non-hydrostatic model (SWASH) was further applied to a wide range of conditions and foreshore slopes to study the energy transfer between frequencies and the corresponding cross-shore evolution of various parameters. Energy balances derived from both the Boussinesq formulation and the Nonlinear Shallow Water Equations (NLSWE) are used to compute interactions between three frequency bands with the NLSWE balance showing most realistic energy transfer for both lower and higher harmonics.

The offshore wave steepness ($s_{m-1,0,\text{deep}}$) and the relative water depth (kh) emerged as the key parameters influencing the energy transfer. When combined with kh and $s_{m-1,0,\text{deep}}$, the Iribarren number (ξ) captures the influence of the slope on several biphases. In the simulations, a transition is observed around $\xi = 0.2$ for biphases associated with low-frequency waves, with larger values in the surf zone for $\xi > 0.2$. In contrast, the biphases related to higher harmonics show a more gradual dependence on ξ. Furthermore, for $\xi < 0.2$, energy from low-frequency components $\left(f < 0.5f_p\right)$ is transferred back to higher frequencies, whereas for steeper foreshore slopes, the low-frequency range predominantly receives energy, in agreement with previous studies.

Results indicate that the generation of low-frequency waves are primarily governed by triad interactions involving two primary components and one low-frequency component, consistent with previous findings. However, for $kh < 0.5$, triads comprising two higher harmonics $\left(f > 1.5f_p\right)$ and one low-frequency components also play a significant role, contributing up to 50% of the total low-frequency energy transfer. Moreover, in the surf zone, energy is redistributed toward higher frequencies mainly by an interaction between two primary components and one high-frequency component or one primary component and two high-frequency components for a $kh < 0.5$.

A consequence of these interactions between frequencies, the wave height of the primary waves reduces as the kh decreases while both low- and high-frequency wave heights increase, particularly under low steepness conditions. For the studied wave conditions, milder foreshore slopes ($\xi < 0.2$) result in low-frequency wave heights up to 60% of the total wave height, whereas the steeper foreshore slopes ($\xi > 0.2$) result in a contribution of the LF waves of 20%–40%. The high frequency contribution varies less with the foreshore slope and offshore conditions and becomes approximately 60%–70% of the total wave height in shallow water. This redistribution and dissipation of energy significantly influence the spectral period, 2% exceedance wave height, and wave steepness. Specifically, the wave steepness based on the spectral period (excluding low-frequency energy) decreases. The relationship between the 2% exceedance wave height and the short wave height shows that, depending on the steepness and foreshore slope, the nearshore time series can be completely different.

Overall, the selected non-hydrostatic wave models perform well in simulating wave propagation over a shallow foreshore and provide insights into the mechanisms driving energy redistribution across frequencies. Thus, these numerical models are useful tools for determining nearshore wave conditions, which are essential for applications such as designing coastal structures. In addition, the simulations show that the nearshore wave conditions can be different depending on the foreshore slope or offshore wave conditions, making it relevant to include time-domain parameters compared to the bulk parameters typically applied in design formulas for coastal structures. Future research should explore how directional spreading influences wave shape and energy transfer, as current findings are derived for long-crested wave conditions.

Appendix A: Bichromatic Wave

To illustrate the relationship between energy distribution and wave correlations, a bichromatic wave condition was simulated over a 1:100 foreshore slope, using frequencies $f_1 = 0.5$ Hz and $f_2 = 0.6$ Hz, with equal amplitudes $a_1 = a_2 = 0.01$ m. In Figure A1, the energy density spectrum and bispectrum are shown for three locations, while Figure A2 shows the normalized energy transfer of various triads along with the corresponding asymmetry ($A_{s,*,*,*}$), skewness ($S_{k,*,*,*}$), biphase $(\phi_{*,*,*})$ and bicoherence ($B_{*,*,*}$). Note that two axis are applied to show the various nonlinear energy transfers (solid lines left axis and dashed lines right axis).

As the water depth decreases several interactions emerge resulting in higher and lower harmonics in the spectrum. The most significant energy transfer occurs from the primary frequencies (f_1 and f_2) to higher harmonics ($2f_1$, $2f_2$ and $f_1 + f_2$) represented by the interaction term $s_{nl,p,p,HH}$. The biphase of this interaction $(\phi_{p,p,HH})$ is approximately $-17/-20°$ with mainly a large skewed signal and relatively low asymmetry. The large bicoherence for the three panels shows that this correlation keeps strong in the domain.

Next to energy to higher harmonics, also energy is redistributed to lower frequencies with $s_{nl,p,p,LF}$, where energy from f_1 and f_2 is transferred to $f_2 - f_1$. The biphase of this interaction changes as the water depth decreases from $-160°$ to $90°$. In deep water the η_{LF} is approximately out of phase with the two primary waves (negative asymmetry and skewness of $\eta_p\eta_p\eta_{LF}$), while this biphase rotates when the water depth decreases. In very shallow water energy from the $f_2 - f_1$ is transferred to $2(f_2 - f_1)$ by $s_{nl,LF,LF,LF}$, resulting in a nonlinear low-frequency signal ($A_{s,LF,LF,LF}$ become negative). Also energy from the higher harmonics ($2f_1$, $2f_2$ and $f_1 + f_2$) is transfers to the lower frequencies $(f_2 - f_1)$ by $s_{nl,HH,HH,LF}$ and $s_{nl,HH,HH,p}$ distributes energy from primary and secondarily peaks to even higher frequencies. The energy distribution with the high frequency range is low (bicoherence lower than 0.5).

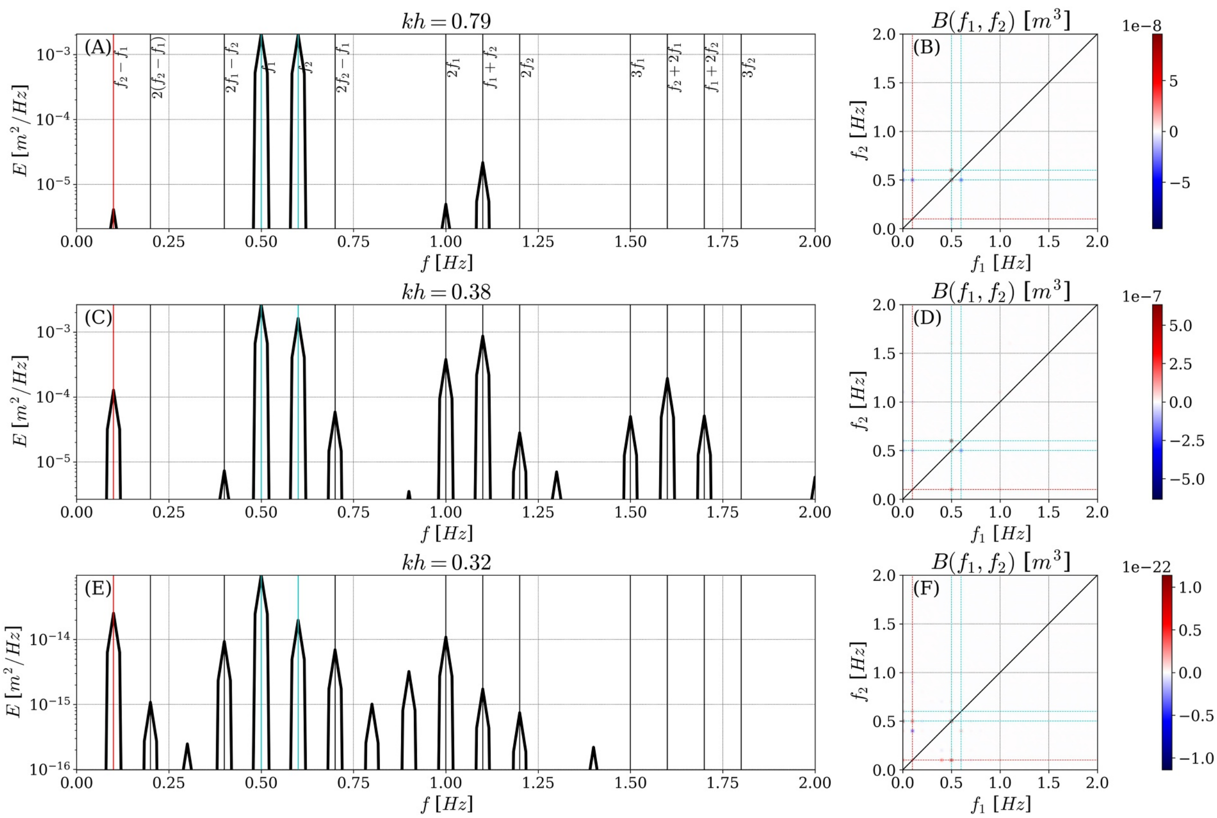

Figure A1. Energy density spectrum (Panels a, c, and e) and bispectrum (Panels b, d, and f) for various water depths. The vertical lines show the interactions involved in the peaks.

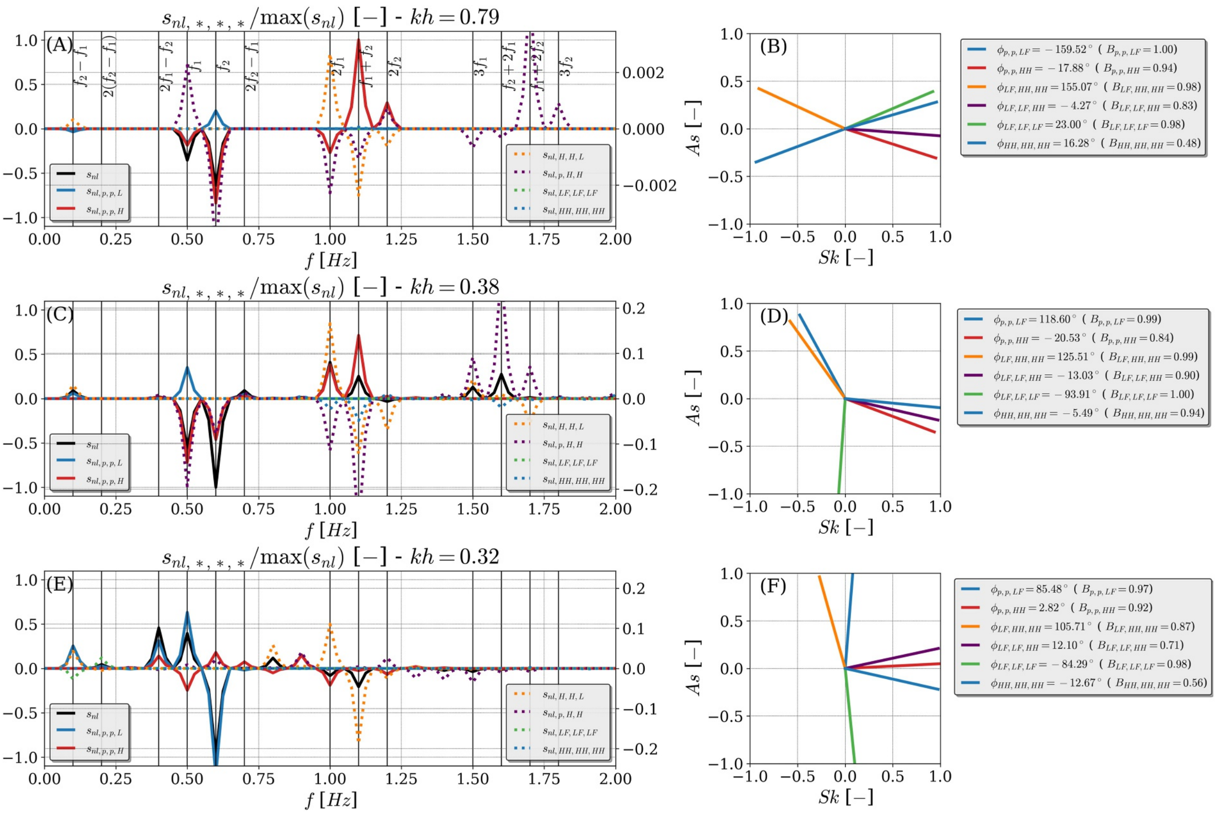

Figure A2. Normalized nonlinear energy transfer for various combinations as function of the frequency (Panels a, c, and e) and the corresponding biphases represented as complex numbers (Panels b, d, and f). Solid normalized nonlinear transfers matched with the left axis and dashed lines match with the right axis.

In the bispectrum the dominant interactions such as ($s_{nl,p,p,LF}$, $s_{nl,p,p,HH}$) are clearly visible with peaks at (f_1,f_1), (f_2,f_2) and (f_1,f_2) as a consequence of $s_{nl,p,p,HH}$ and peak at $(f_1,f_2 - f_1)$ as a consequence of $s_{nl,p,p,LF}$. Other interactions with significantly lower energy are not detectable in the bispectrum.

These results help clarify the behavior observed under irregular wave conditions, enabling a direct link between energy at specific frequencies and the corresponding nonlinear interactions. These findings are consistent with the irregular waves, mainly that both primary waves and high frequency waves transfer energy to the lower frequencies. Also the dominant interactions match with the observations for the irregular wave conditions.

Appendix B: Consistently Check

To verify the implementation of the third-order statistics and the nonlinear source term, both the formulation from the bispectrum and in the time domain are compared as a consistency check in Figure B1. The skewness and asymmetry obtained from the bispectrum (see, e.g., (Elgar & Guza, 1985a)) closely match the values calculated in the time domain (Equations 2 and 3), confirming that the bispectrum is accurately estimated. Similarly, the nonlinear source term based on Boussinesq theory (S_{nl}) shows strong agreement between the time-domain computation (Equation 11) and the bispectrum-based approach (see, e.g., (De Bakker et al., 2015; Herbers & Burton, 1997; Herbers et al., 2000; Smit et al., 2014)). Small deviations in the $S_{nl,f}$ may result from differences in the estimation of be bispectrum (e.g., different frequency resolution). Overall, these comparisons demonstrate that the current implementation is consistent with bispectrum-based analysis.

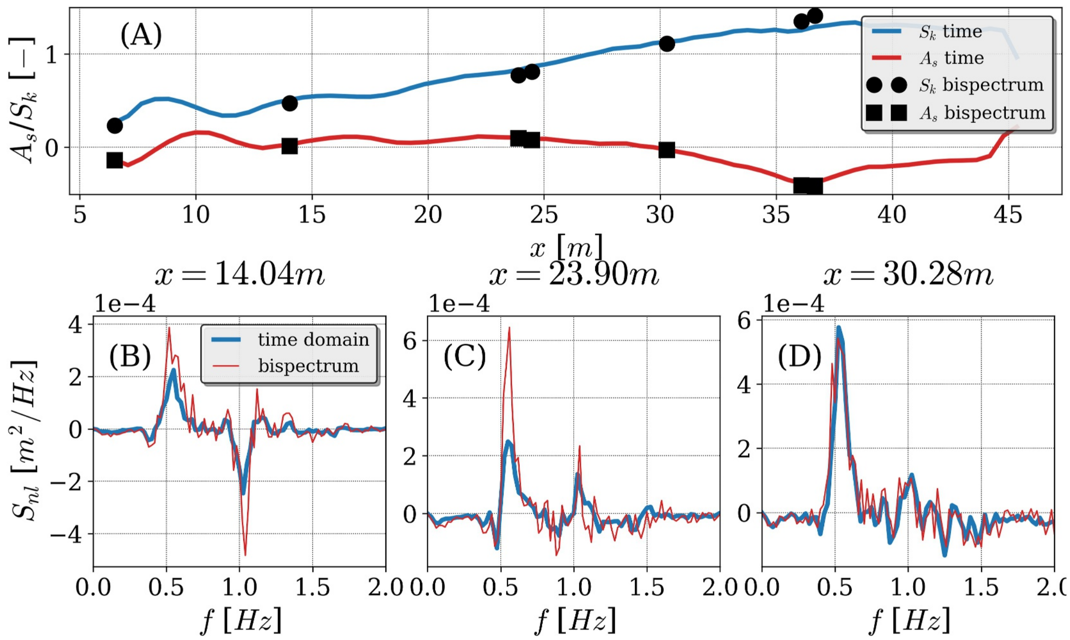

Figure B1. Comparison of asymmetry and skewness computed with Equations 2 and 3 and based on the bispectrum (Panel a). Panel (b–d) show the comparisons of $S_{nl,f}$ between the analysis based on Equation 11 and based on the bispectrum for several locations. Results are obtained from test CA711.

Appendix C: Validation

See Figure C1

See Figure C2

See Figure C3

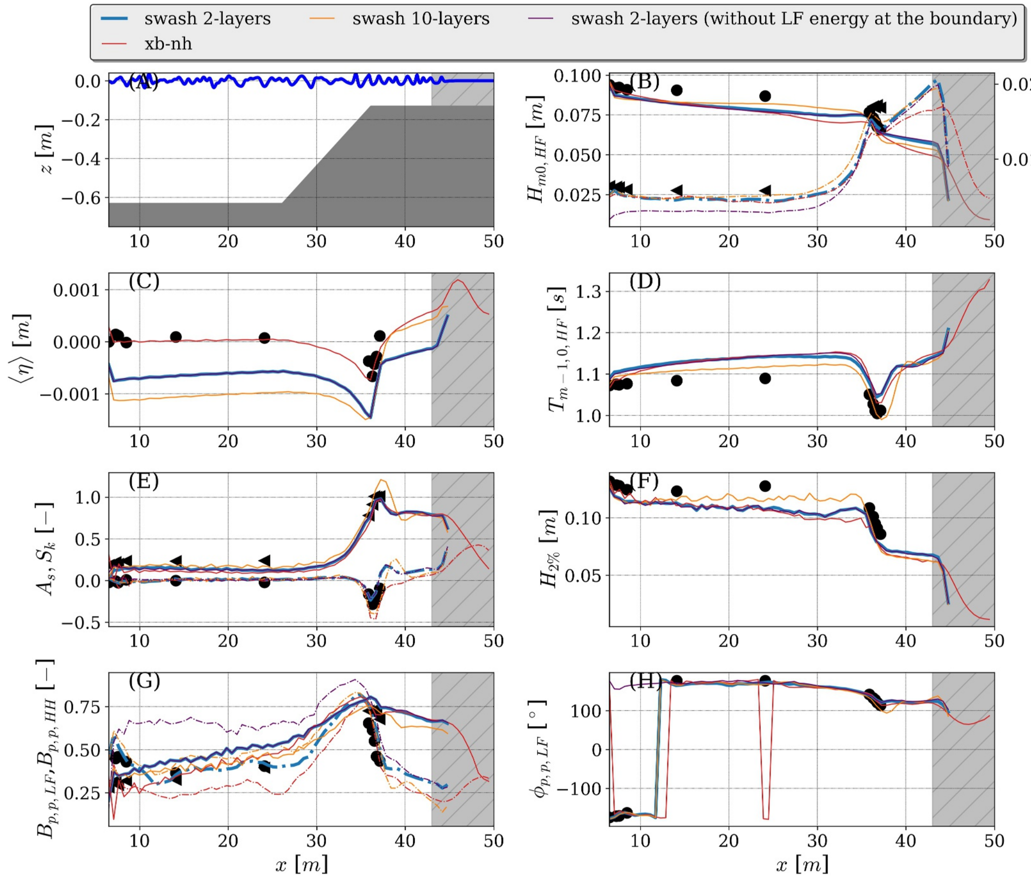

Figure C1. Comparison of short wave height ($H_{m0,HF}$, Panel b), low-frequency wave height ($H_{m0,LF}$, Panel b, dashed lines), wave setup ($\langle\eta\rangle$, Panel c), short wave spectral period ($T_{m-1,0,HF}$, Panel d), wave asymmetry (A_s, Panel e), wave skewness (S_k, Panel e, dashes lines), 2% exceedance wave height ($H_{2\%}$, Panel f), bicoherence of signal involving two primary waves and one low-frequency wave ($B_{p,p,LF}$, Panel g), bicoherence of signal involving two primary waves and one higher harmonic ($B_{p,p,HH}$, Panel g, dashed lines) and biphase of signal involving two primary waves and one low-frequency wave ($\phi_{p,p,LF}$, Panel h) for various models for Test CC713. The black dots show the observations from the wave flume experiments. The low-frequency height, skewness and $B_{p,p,HH}$ are shown with a dashed line and triangles for the observations. The sponge layer is indicated with a gray shaded area.

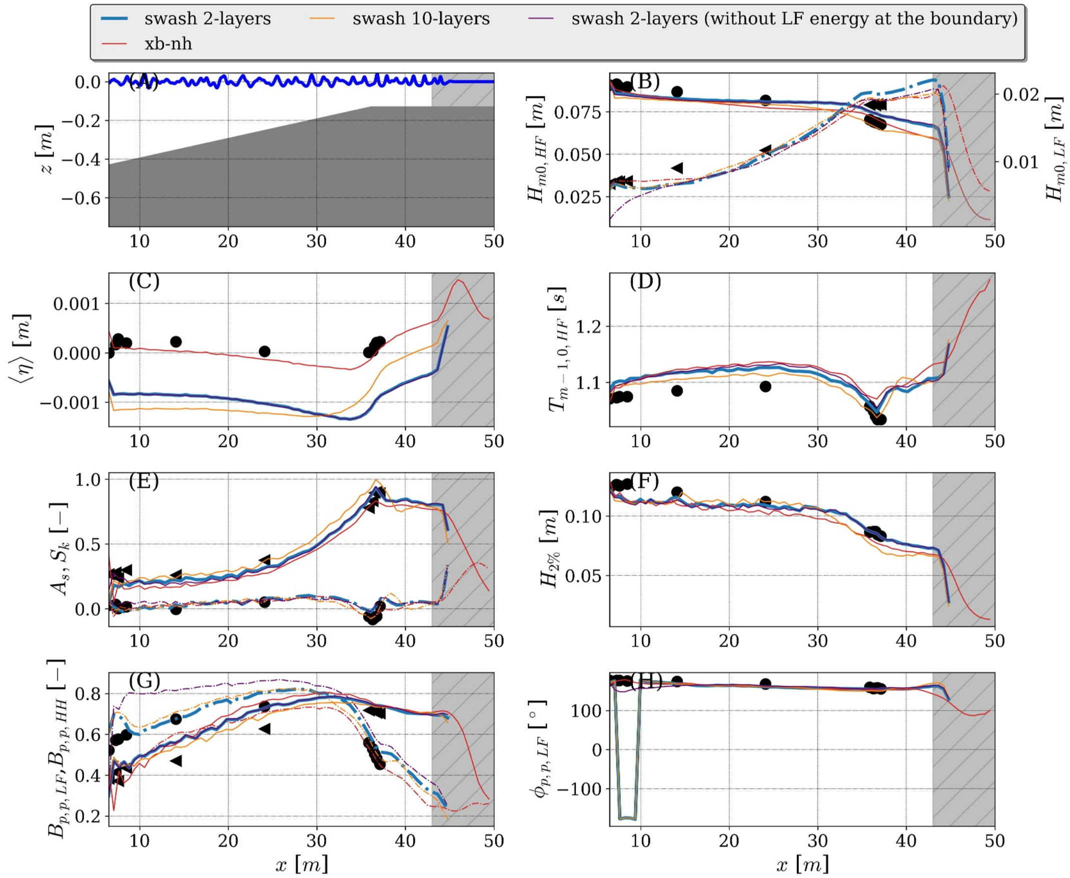

Figure C2. Comparison of short wave height ($H_{m0,HF}$, Panel b), low-frequency wave height ($H_{m0,LF}$, Panel b, dashed lines), wave setup ($\langle\eta\rangle$, Panel c), short wave spectral period ($T_{m-1,0,HF}$, Panel d), wave asymmetry (A_s, Panel e), wave skewness (S_k, Panel e, dashes lines), 2% exceedance wave height ($H_{2\%}$, Panel f), bicoherence of signal involving two primary waves and one low-frequency wave ($B_{p,p,LF}$, Panel g), bicoherence of signal involving two primary waves and one higher harmonic ($B_{p,p,HH}$, Panel g, dashed lines) and biphase of signal involving two primary waves and one low-frequency wave ($\phi_{p,p,LF}$, Panel h) for various models for Test CA713. The black dots show the observations from the wave flume experiments. The low-frequency height, skewness and $B_{p,p,HH}$ are shown with a dashed line and triangles for the observations. The sponge layer is indicated with a gray shaded area.

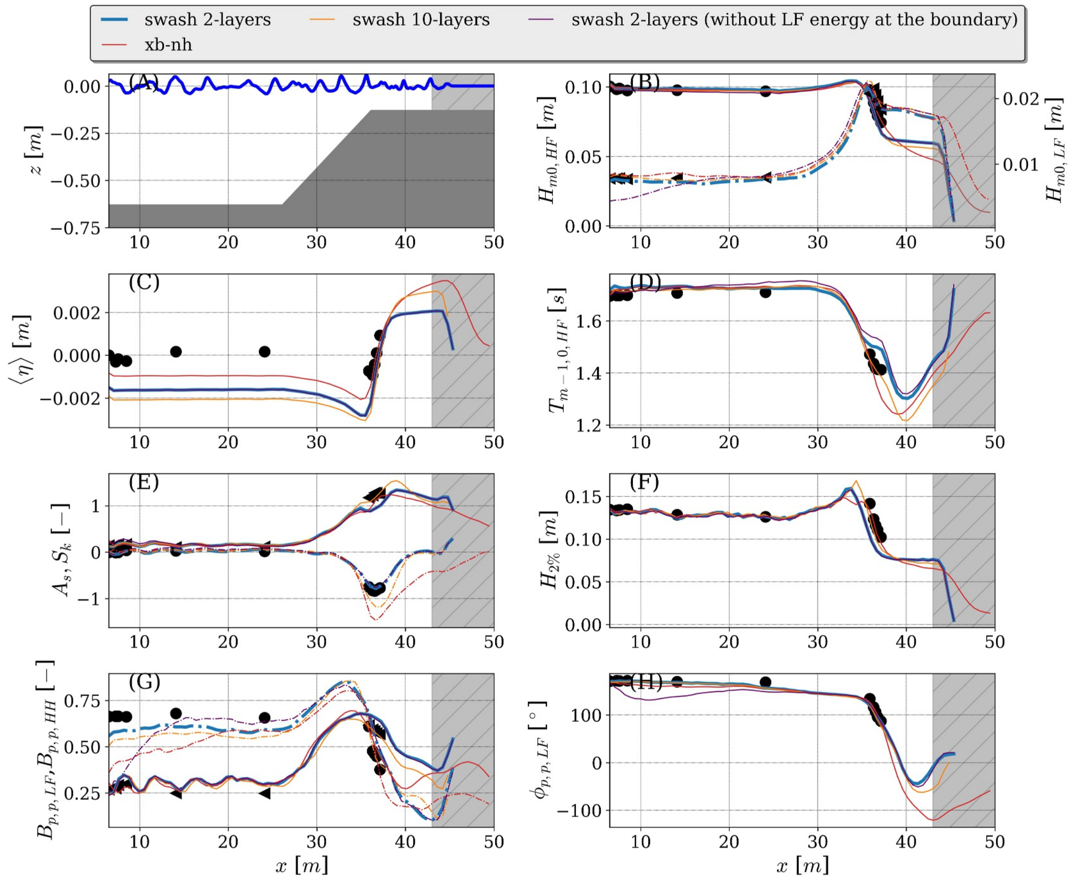

Figure C3. Comparison of short wave height ($H_{m0,HF}$, Panel b), low-frequency wave height ($H_{m0,LF}$, Panel b, dashed lines), wave setup ($\langle\eta\rangle$, Panel c), short wave spectral period ($T_{m-1,0,HF}$, Panel d), wave asymmetry (A_s, Panel e), wave skewness (S_k, Panel e, dashes lines), 2% exceedance wave height ($H_{2\%}$, Panel f), bicoherence of signal involving two primary waves and one low-frequency wave ($B_{p,p,LF}$, Panel g), bicoherence of signal involving two primary waves and one higher harmonic ($B_{p,p,HH}$, Panel g, dashed lines) and biphase of signal involving two primary waves and one low-frequency wave ($\phi_{p,p,LF}$, Panel h) for various models for Test CC711. The black dots show the observations from the wave flume experiments. The low-frequency height, skewness and $B_{p,p,HH}$ are shown with a dashed line and triangles for the observations. The sponge layer is indicated with a gray shaded area.

Appendix D: Validation of Time Series

In Figures D1 and D2 the simulated and observed time series for one of the tests are compared for an offshore and nearshore location showing a good match between model and observations.

10.1029/2025JC023751

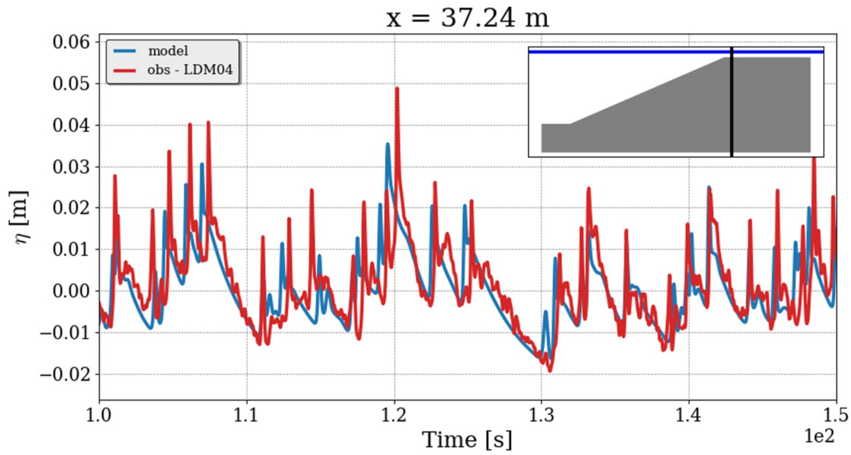

Figure D1. Time series at offshore location.

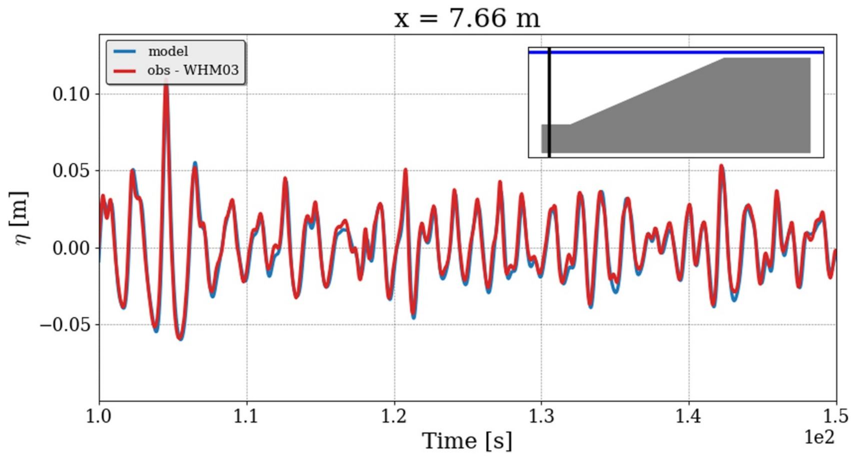

Figure D2. Time series at nearshore location.

Conflict of Interest

The authors declare no conflicts of interest relevant to this study.

Availability Statement

The open-source numerical models SWASH and XBeach are available at https://swash.sourceforge.io/ and https://download.deltares.nl/xbeach, respectively. The model input files used in this study, together with the observational data employed for model validation, are publicly available at https://doi.org/10.4121/491d2285-8c53-4950-90f5-d6f78739198f.

Acknowledgments

This study was realized with the help of a TKI (Top Consortia for Knowledge and Innovation) subsidy (Delta Technology project CLIMACS, project DEL171) and the support by the "Vereniging van Waterbouwers".

References

Al Khalili, U., Bellos, V., Christou, M., & Karmpadakis, I. (2025). Regular and random wave modelling over mild uniform bathymetry using swash. *Coastal Engineering*, *199*, 104745. https://doi.org/10.1016/j.coastaleng.2025.104745

Baldock, T. E. (2012). Dissipation of incident forced long waves in the surf zone—Implications for the concept of "bound" wave release at short wave breaking. *Coastal Engineering*, *60*, 276–285. https://doi.org/10.1016/j.coastaleng.2011.11.002

Baldock, T. E., & Huntley, D. A. (2002). Long–wave forcing by the breaking of random gravity waves on a beach. *Proceedings of the Royal Society of London Series A: Mathematical, Physical and Engineering Sciences*, *458*(2025), 2177–2201. https://doi.org/10.1098/rspa.2002.0962

Battjes, J. A. (1974). Surf similarity. In *Coastal engineering 1974* (Vol. 7, pp. 466–480). American Society of Civil Engineers. https://doi.org/10.1061/9780872621138.029

Battjes, J. A., Bakkenes, H. J., Janssen, T. T., & Van Dongeren, A. R. (2004). Shoaling of subharmonic gravity waves. *Journal of Geophysical Research*, *109*(C2). https://doi.org/10.1029/2003JC001863

Bonneton, P. (2023). Energy and dissipation spectra of waves propagating in the inner surf zone. *Journal of Fluid Mechanics*, *977*, A48. https://doi.org/10.1017/jfm.2023.878

De Bakker, A., Tissier, M., & Ruessink, B. (2014). Shoreline dissipation of infragravity waves. *Continental Shelf Research*, *72*, 73–82. https://doi.org/10.1016/j.csr.2013.11.013

De Bakker, A. T. M., Herbers, T. H. C., Smit, P. B., Tissier, M. F. S., & Ruessink, B. G. (2015). Nonlinear infragravity–wave interactions on a gently sloping laboratory beach. *Journal of Physical Oceanography*, *45*(2), 589–605. https://doi.org/10.1175/JPO-D-14-0186.1

De Bakker, A. T. M., Tissier, M. F. S., & Ruessink, B. G. (2016). Beach steepness effects on nonlinear infragravity-wave interactions: A numerical study. *Journal of Geophysical Research: Oceans*, *121*(1), 554–570. https://doi.org/10.1002/2015JC011268

Den Bieman, J., De Ridder, M., & Doeleman, M. (2024). Validation of an efficient two-layer non-hydrostatic wave model on a sloping foreshore. *Journal of Coastal and Hydraulic Structures*, *4*. https://doi.org/10.59490/jchs.2024.0038

De Ridder, M. P., Kramer, J., Den Bieman, J. P., & Wenneker, I. (2023). Validation and practical application of nonlinear wave decomposition methods for irregular waves. *Coastal Engineering*, *183*, 104311. https://doi.org/10.1016/j.coastaleng.2023.104311

De Ridder, M. P., Smit, P. B., Van Dongeren, A. R., McCall, R. T., Nederhoff, K., & Reniers, A. J. H. M. (2021). Efficient two-layer non-hydrostatic wave model with accurate dispersive behaviour. *Coastal Engineering*, *164*, 103808. https://doi.org/10.1016/j.coastaleng.2020.103808

De Ridder, M. P., Van Kester, D. C. P., Van Bentem, R., Teng, D. Y. Y., & Van Gent, M. R. A. (2024). Wave overtopping discharges at rubble mound structures in shallow water. *Coastal Engineering*, *194*, 104626. https://doi.org/10.1016/j.coastaleng.2024.104626

De Wit, F., Tissier, M., & Reniers, A. (2020). The relationship between sea-swell bound wave height and wave shape. *Journal of Marine Science and Engineering*, *8*(9), 643. https://doi.org/10.3390/jmse8090643

Elgar, S., & Guza, R. T. (1985a). Observations of bispectra of shoaling surface gravity waves. *Journal of Fluid Mechanics*, *161*(1), 425–448. https://doi.org/10.1017/S0022112085003007

Elgar, S., & Guza, R. T. (1985b). Shoaling gravity waves: Comparisons between field observations, linear theory, and a nonlinear model. *Journal of Fluid Mechanics*, *158*, 47–70. https://doi.org/10.1017/S0022112085002543

Fiedler, J. W., Smit, P. B., Brodie, K. L., McNinch, J., & Guza, R. T. (2019). The offshore boundary condition in surf zone modeling. *Coastal Engineering*, *143*, 12–20. https://doi.org/10.1016/j.coastaleng.2018.10.014

Freilich, M. H., & Guza, R. T. (1984). Nonlinear effects on shoaling surface gravity waves. *Philosophical Transactions of the Royal Society of London. Series A, Mathematical and Physical Sciences*, *311*(1515), 1–41. https://doi.org/10.1098/rsta.1984.0019

Hasselmann, K. (1962). On the non-linear energy transfer in a gravity-wave spectrum part 1. General theory. *Journal of Fluid Mechanics*, *12*(4), 481–500. https://doi.org/10.1017/S0022112062000373

Hasselmann, K., Munk, W., & MacDonald, G. J. (1963). Bispectra of ocean waves. In *Symposium on Time Series Analysis* (pp. 125–139).

Henderson, C. S., Fiedler, J. W., Merrifield, M. A., Guza, R. T., & Young, A. P. (2022). Phase resolving runup and overtopping field validation of swash. *Coastal Engineering*, *175*, 104128. https://doi.org/10.1016/j.coastaleng.2022.104128

Henderson, S. M., Guza, R. T., Elgar, S., Herbers, T. H. C., & Bowen, A. J. (2006). Nonlinear generation and loss of infragravity wave energy. *Journal of Geophysical Research*, *111*(C12). https://doi.org/10.1029/2006JC003539

Herbers, T. H. C., & Burton, M. C. (1997). Nonlinear shoaling of directionally spread waves on a beach. *Journal of Geophysical Research*, *102*(C9), 21101–21114. https://doi.org/10.1029/97JC01581

Herbers, T. H. C., & Guza, R. T. (1994). Nonlinear wave interactions and high-frequency seafloor pressure. *Journal of Geophysical Research*, *99*(C5), 10035–10048. https://doi.org/10.1029/94JC00054

Herbers, T. H. C., Russnogle, N. R., & Elgar, S. (2000). Spectral energy balance of breaking waves within the surf zone. *Journal of Physical Oceanography*, *30*(11), 2723–2737. https://doi.org/10.1175/1520-0485(2000)030⟨2723:SEBOBW⟩2.0.CO;2

Janssen, T. T., Battjes, J. A., & Van Dongeren, A. R. (2003). Long waves induced by short-wave groups over a sloping bottom. *Journal of Geophysical Research*, *108*(C8). https://doi.org/10.1029/2002JC001515

Klopman, G., & Dingemans, M. W. (2001). Wave interactions in the coastal zone. In *Proceedings 16th International Workshop on Water Waves and Floating Bodies*.

Lamb, H. (1932). *Hydrodynamics* (6th ed.). Cambridge University Press.

Lashley, C. H., Van der Meer, J., Bricker, J. D., Altomare, C., Suzuki, T., & Hirayama, K. (2021). Formulating wave overtopping at vertical and sloping structures with shallow foreshores using deep-water wave characteristics. *Journal of Waterway, Port, Coastal, and Ocean Engineering*, *147*(6), 04021036. https://doi.org/10.1061/(ASCE)WW.1943-5460.0000675

Lashley, C. H., Zanuttigh, B., Bricker, J. D., Van der Meer, J., Altomare, C., Suzuki, T., et al. (2020). Benchmarking of numerical models for wave overtopping at dikes with shallow mildly sloping foreshores: Accuracy versus speed. *Environmental Modelling and Software*, *130*, 104740. https://doi.org/10.1016/j.envsoft.2020.104740

Longuet-Higgins, M. S., & Stewart, R. W. (1962). Radiation stress and mass transport in gravity waves, with application to a surf beat. *Journal of Fluid Mechanics*, *13*(4), 481–504. https://doi.org/10.1017/S0022112062000877

Martins, K., Bonneton, P., & Michallet, H. (2021). Dispersive characteristics of non-linear waves propagating and breaking over a mildly sloping laboratory beach. *Coastal Engineering*, *167*, 103917. https://doi.org/10.1016/j.coastaleng.2021.103917

Mendes, D., Pinto, J. P., Pires-Silva, A. A., & Fortunato, A. B. (2018). Infragravity wave energy changes on a dissipative barred beach: A numerical study. *Coastal Engineering*, *140*, 136–146. https://doi.org/10.1016/j.coastaleng.2018.07.005

Norheim, C. A., Herbers, T. H. C., & Elgar, S. (1998). Nonlinear evolution of surface wave spectra on a beach. *Journal of Physical Oceanography*, *28*(7), 1534–1551. https://doi.org/10.1175/1520-0485(1998)028<1534:neosws>2.0.co;2

Padilla, E. M., & Alsina, J. M. (2017). Transfer and dissipation of energy during wave group propagation on a gentle beach slope. *Journal of Geophysical Research: Oceans*, *122*(8), 6773–6794. https://doi.org/10.1002/2017JC012703

Peregrine, D. H. (1983). Breaking waves on beaches. *Annual Review of Fluid Mechanics*, *15*(1), 149–178. https://doi.org/10.1146/annurev.fl.15.010183.001053

Rijnsdorp, D. P., Smit, P. B., & Guza, R. T. (2022). A nonlinear, non-dispersive energy balance for surf zone waves: Infragravity wave dynamics on a sloping beach. *Journal of Fluid Mechanics*, *944*, A45. https://doi.org/10.1017/jfm.2022.512

Rijnsdorp, D. P., Smit, P. B., & Zijlema, M. (2014). Non-hydrostatic modelling of infragravity waves under laboratory conditions. *Coastal Engineering*, *85*, 30–42. https://doi.org/10.1016/j.coastaleng.2013.11.011

Rocha, M., Michallet, H., & Silva, P. (2017). Improving the parameterization of wave nonlinearities—The importance of wave steepness, spectral bandwidth and beach slope. *Coastal Engineering*, *121*, 77–89. https://doi.org/10.1016/j.coastaleng.2016.11.012

Roelvink, D., McCall, R., Mehvar, S., Nederhoff, K., & Dastgheib, A. (2018). Improving predictions of swash dynamics in xbeach: The role of groupiness and incident-band runup. *Coastal Engineering*, *134*, 103–123. https://doi.org/10.1016/j.coastaleng.2017.07.004
Ruju, A., Lara, J. L., & Losada, I. J. (2019). Numerical assessment of infragravity swash response to offshore wave frequency spread variability. *Journal of Geophysical Research: Oceans*, *124*(9), 6643–6657. https://doi.org/10.1029/2019JC015063
Sheremet, A., Guza, R. T., Elgar, S., & Herbers, T. H. C. (2002). Observations of nearshore infragravity waves: Seaward and shoreward propagating components. *Journal of Geophysical Research*, *107*(C8). https://doi.org/10.1029/2001JC000970
Smit, P., Janssen, T., Holthuijsen, L., & Smith, J. (2014). Non-hydrostatic modeling of surf zone wave dynamics. *Coastal Engineering*, *83*, 36–48. https://doi.org/10.1016/j.coastaleng.2013.09.005
Smit, P., Zijlema, M., & Stelling, G. (2013). Depth-induced wave breaking in a non-hydrostatic, near-shore wave model. *Coastal Engineering*, *76*, 1–16. https://doi.org/10.1016/j.coastaleng.2013.01.008
Stoker, J. J. (1992). *Water waves: The mathematical theory with applications*. John Wiley and Sons, Ltd.
Suzuki, T., Altomare, C., Veale, W., Verwaest, T., Trouw, K., Troch, P., & Zijlema, M. (2017). Efficient and robust wave overtopping estimation for impermeable coastal structures in shallow foreshores using swash. *Coastal Engineering*, *122*, 108–123. https://doi.org/10.1016/j.coastaleng.2017.01.009
Svendsen, I. A., Madsen, P. A., & Hansen, J. B. (1978). Wave characteristics in the surf zone (pp. 520–539). https://doi.org/10.1061/9780872621909.031
Symonds, G., Huntley, D. A., & Bowen, A. J. (1982). Two-dimensional surf beat: Long wave generation by a time-varying breakpoint. *Journal of Geophysical Research*, *87*(C1), 492–498. https://doi.org/10.1029/JC087iC01p00492
Thornton, E. B., & Guza, R. T. (1982). Energy saturation and phase speeds measured on a natural beach. *Journal of Geophysical Research*, *87*(C12), 9499–9508. https://doi.org/10.1029/JC087iC12p09499
Torres-Freyermuth, A., Lara, J. L., & Losada, I. J. (2010). Numerical modelling of short- and long-wave transformation on a barred beach. *Coastal Engineering*, *57*(3), 317–330. https://doi.org/10.1016/j.coastaleng.2009.10.013
Van den Hoven, K., Van Belzen, J., Kleinhans, M. G., Schot, D. M. J., Merry, J., Van Loon-Steensma, J. M., & Bouma, T. J. (2023). How natural foreshores offer flood protection during dike breaches: An explorative flume study. *Estuarine Coastal and Shelf Science*, *294*, 108560. https://doi.org/10.1016/j.ecss.2023.108560
Van Dongeren, A., Battjes, J., Janssen, T., van Noorloos, J., Steenhauer, K., Steenbergen, G., & Reniers, A. (2007). Shoaling and shoreline dissipation of low-frequency waves. *Journal of Geophysical Research*, *112*(C2). https://doi.org/10.1029/2006JC003701
Van Gent, M. R. A. (2001). Wave runup on dikes with shallow foreshores. *Journal of Waterway, Port, Coastal, and Ocean Engineering*, *127*(5), 254–262. https://doi.org/10.1061/(ASCE)0733-950X(2001)127:5(254)
Van Gent, M. R. A. (2019). Climate adaptation of coastal structures. In *Proceedings of the SCACR19 9th Short Course/Conference on Applied Coastal Research, Bari, Italy* (pp. 9–11).
Van Gent, M. R. A., & Teng, D. Y. Y. (2023). Climate adaptation of coastal structures: Application of adaptation pathways for rubble mound breakwaters. In *Proceedings PIANC-COPEDEC X*.
Vasarmidis, P., Klonaris, G., Zijlema, M., Stratigaki, V., & Troch, P. (2024). A study of the non-linear properties and wave generation of the multi-layer non-hydrostatic wave model swash. *Ocean Engineering*, *302*, 117633. https://doi.org/10.1016/j.oceaneng.2024.117633
Vuik, V., Jonkman, S. N., Borsje, B. W., & Suzuki, T. (2016). Nature-based flood protection: The efficiency of vegetated foreshores for reducing wave loads on coastal dikes. *Coastal Engineering*, *116*, 42–56. https://doi.org/10.1016/j.coastaleng.2016.06.001
Welch, P. (1967). The use of fast fourier transform for the estimation of power spectra: A method based on time averaging over short, modified periodograms. *IEEE Transactions on Audio and Electroacoustics*, *15*(2), 70–73. https://doi.org/10.1109/TAU.1967.1161901
Zijlema, M., Stelling, G., & Smit, P. (2011). Swash: An operational public domain code for simulating wave fields and rapidly varied flows in coastal waters. *Coastal Engineering*, *58*(10), 992–1012. https://doi.org/10.1016/j.coastaleng.2011.05.015